

# Basis of Atomic Diffusion

Kazuhiko Sasagawa and Masumi Saka

**Abstract** Atomic diffusion, or more specifically, electromigration (EM) and stress migration (SM), are described in this chapter. The driving force of atomic diffusion is electron wind in EM and the gradient of hydrostatic stress in SM. In [Sect. 1](#), the fundamental principles of EM are presented. For actual metal lines, which may have various microstructures and be covered with a passivation layer, EM behavior is explained. Then, a method for calculating the divergence of atomic flux due to EM is introduced, and the formulation process is described to help readers understand the application of the calculation method. The formula of the divergence *AFD* describes the behavior of EM damage well, which affects the reliability of silicon integrated circuits. Based on the *AFD* formula, a method for deriving the characteristic constants of EM in the line is introduced. In [Sect. 2](#), the basic principles of SM are given through a brief review of typical SM-induced phenomena. The current research trends regarding nanomaterial production using SM and the mechanism of the production are discussed.

---

K. Sasagawa (✉)

Department of Intelligent Machines and System Engineering, Hirosaki University,  
3 Bunkyo-cho, Hirosaki 036-8561, Japan  
e-mail: sasagawa@cc.hirosaki-u.ac.jp

M. Saka

Department of Nanomechanics, Tohoku University, Aoba 6-6-01, Aramaki, Aoba-ku,  
Sendai 980-8579, Japan  
e-mail: saka@ism.mech.tohoku.ac.jp

## 1 Electromigration

### 1.1 Historical Review of EM

An electric field has long been known to induce the motion of ions in metals [23]. In 1961, Huntington and Grone reported the EM phenomenon of current-induced motion of scratches on a metal surface [37]. EM has been described as the transport of metal atoms, driven by momentum transfer from electron flow. Huntington and Grone proposed an equation (now known as the Huntington–Grone equation) that describes atomic flow. EM was first observed in bulk metals. In the late 1960s, EM was recognized as a failure mechanism of integrated circuits (ICs) [10]. Black [5] systematically studied EM in IC metal lines. The damage induced by EM is manifest as voids and hillocks, which are formed by the depletion and accumulation of metal atoms, respectively. The growth and linking of voids results in electrical discontinuity in the IC metal lines, which in turn leads to open-circuit failure. The lifetime of the metal line is primarily governed by EM damage, and therefore must be predicted quantitatively to ensure the reliability of ICs. Black formulated an empirical equation for predicting the mean time to failure, *MTF*. Black’s equation is given by

$$MTF = Aj^{-n} \exp\left(\frac{Q}{kT}\right), \quad (1)$$

where  $A$  is a constant related to the line shape and line material,  $j$  is the input current density,  $n$  is the order of current density dependence,  $Q$  is the activation energy,  $k$  is the Boltzmann constant, and  $T$  is the absolute temperature. Today, this equation remains widely used to predict the lifetime of IC interconnects. Since the 1980s, EM has been extensively researched with respect to the reliability of ICs, because EM, along with SM, is recognized as the main failure mechanism. EM in IC metal lines has been studied numerically to predict the lifetime and failure site of the lines [1, 40, 45, 46, 58, 62]. Recently, Cu has begun to replace Al as a line material. In comparison with Al, Cu is expected to be more robust against EM failure; nevertheless, EM failure remains a major issue affecting the reliability of modern ICs.

### 1.2 Theory of EM (Huntington–Grone Equation)

Atomic diffusion in metal can be considered the diffusion of ionized particles [65]. The diffusion velocity  $v$  of the ionized particles caused by external force is given by

$$v = \beta F, \quad (2)$$

where  $\beta$  is mobility and  $\mathbf{F}$  is the driving force. According to the Nernst–Einstein equation,  $\beta$  is expressed by

$$\beta = \frac{D}{kT}. \quad (3)$$

Here,  $D$  is the diffusion coefficient given by

$$D = D_0 \exp\left(-\frac{Q}{kT}\right), \quad (4)$$

where  $D_0$  is prefactor.

The relationship between the flux of particles (i.e., the number of particles passing through a unit area per unit time) and the velocity of particles is given by

$$\mathbf{J} = N\mathbf{v}, \quad (5)$$

where  $\mathbf{J}$  is the particle flux and  $N$  is the particle density. For atoms,  $\mathbf{J}$  is the atomic flux and  $N$  is the atomic density. Using Eqs. (2), (3) and (5), the flux of the ionized particles caused by external force is given as

$$\mathbf{J} = \frac{ND}{kT} \mathbf{F}. \quad (6)$$

The driving force  $\mathbf{F}$  consists of two types of forces,  $\mathbf{F}_c$  and  $\mathbf{F}_e$ , in the case of EM.  $\mathbf{F}_c$  is the force acting on an electric charge in electric field  $\mathbf{E}$ , and  $\mathbf{F}_e$  is the force transmitted by electron collisions. The forces  $\mathbf{F}_c$  and  $\mathbf{F}_e$  are simply expressed by

$$\mathbf{F}_c = q\mathbf{E} = C_1 e\mathbf{E} \quad (7)$$

and

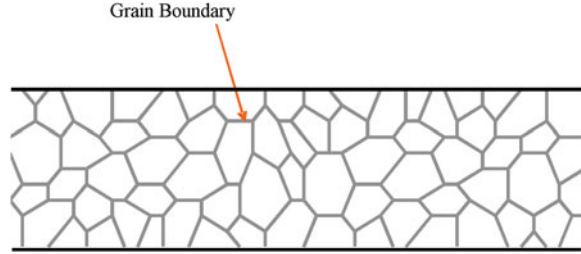
$$\mathbf{F}_e = C_2(-e)\mathbf{E}, \quad (8)$$

where  $q$  is the ionic charge,  $e$  is the charge of an electron, and  $C_1$  and  $C_2$  are proportional constants. Denoting electrical resistivity by  $\rho$  and current density by  $\mathbf{j}$ , electric field  $\mathbf{E}$  is given by  $\rho\mathbf{j}$ , and the driving force  $\mathbf{F}$  is given by

$$\mathbf{F} = \mathbf{F}_c + \mathbf{F}_e = (C_1 - C_2)e\mathbf{E} = Z^*e\rho\mathbf{j}, \quad (9)$$

where  $Z^*$  is the effective valence. Substituting Eq. (9) into Eq. (6), we obtain the Huntington–Grone equation:

$$\mathbf{J} = \frac{ND}{kT} Z^*e\rho\mathbf{j} = \frac{ND_0}{kT} \exp\left(-\frac{Q}{kT}\right) Z^*e\rho\mathbf{j}. \quad (10)$$

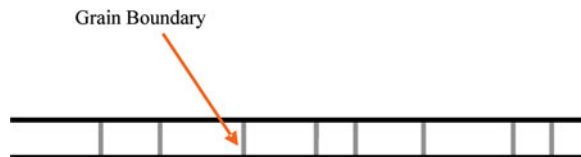
**Fig. 1** Polycrystalline line

### ***1.3 Polycrystalline Structure of Metallic Thin Films***

EM in metal lines occurs along grain boundaries as well as within grains (lattice diffusion). When a metal line width is greater than several micrometers, there are several grains in the width direction. The thickness of a metallic thin film is generally smaller than the grain size. The microstructure of a polycrystalline line is shown in Fig. 1. The main path of atomic diffusion is considered to be along the grain boundaries, and lattice diffusion can be neglected in the case of EM in a polycrystalline line [6], because the diffusion coefficient in grain boundaries is much larger than that in the lattice [57].

### ***1.4 Bamboo Structure in Metallic Thin Films***

If the width of a metal line is less than about 1  $\mu\text{m}$ , there is only one grain in the width direction. Such a metal line has a so-called bamboo structure. The microstructure of a bamboo line is shown in Fig. 2. In the bamboo line, it is assumed that the atomic flux in the grain boundary is negligible [73] and that lattice diffusion [20, 48, 49, 52, 68] including interface diffusion [12, 36, 52, 63] by EM is dominant. This assumption is based on the small number of grain boundaries, which are perpendicular to the longitudinal axis of the line [73, 75]. The velocity of atomic diffusion in a bamboo line is much slower than that in a polycrystalline line, because the diffusion coefficient for the lattice within the grain is much smaller than that for grain boundaries.

**Fig. 2** Bamboo line

## 1.5 Effect of Passivation on EM

Metal lines used in packaged silicon ICs are covered with a passivation layer. In contrast to unpassivated lines, hillock formation is difficult to induce by EM in passivated lines. When hillock formation is suppressed, a gradient of mechanical stress builds up in the line, specifically, compressive stress is generated by atomic density increasing at the anode of the line and tensile stress is generated by atomic density decreasing at the cathode of the line. This gradient induces another form of atomic diffusion, called ‘back flow’, in the opposite direction of EM [7–9]. Consequently, EM in the passivated line is inhibited by the back flow. This also explains why the lifetime of covered metal lines is longer than that of uncovered lines [44, 60].

In a modification of the Huntington–Grone equation (10), the atomic flux in the passivated metal line is assumed to be represented [61] by

$$|\mathbf{J}| = \frac{ND_0}{kT} \exp \left\{ -\frac{Q + \kappa\Omega(N - N_T)/N_0 - \sigma_T\Omega}{kT} \right\} \left( Z^* e \rho j^* - \frac{\kappa\Omega}{N_0} \frac{\partial N}{\partial l} \right), \quad (11)$$

where  $\kappa$  is the effective bulk modulus [42],  $N_T$  is the atomic density under tensile thermal stress  $\sigma_T$ ,  $j^*$  is the component of current density in the direction of  $\mathbf{J}$ ,  $N_0$  is the atomic density at a reference condition,  $\Omega$  is the atomic volume [ $\cong 1/N_0$ ], and  $\rho$  [ $=\rho_0\{1 + \alpha(T - T_s)\}$ ] is the temperature-dependent resistivity;  $\rho_0$  and  $\alpha$ , respectively, are the electrical resistivity and the temperature coefficient at the substrate temperature  $T_s$ .  $\partial N/\partial l$  is the atomic density gradient in the direction of  $\mathbf{J}$ . The effect on diffusivity of the stress generated in the metal line is given by the term  $\kappa\Omega(N - N_T)/N_0 - \sigma_T\Omega$  in the exponential function [2, 50]. On the other hand, the effect of the back flow of atoms induced by an atomic density gradient is given by  $(\kappa\Omega/N_0) \partial N/\partial l$  [7, 8, 42]. These two effects are taken into account in Eq. (11). The quantity  $N_0$  is obtained under stress-free conditions at 300 K [74], and  $N_T$  can be approximated by  $N_0$  [61].

There is a threshold current density of EM damage,  $j_{th}$ , below which no EM damage appears in the case of passivated and via-connected metal lines [9]. When  $|j^*| \leq j_{th}$ , the driving force given in the last set of parentheses in Eq. (11) vanishes because the driving force of EM induced by  $j^*$  and that of back flow induced by  $\partial N/\partial l$  are balanced.

## 1.6 Governing Parameter for EM Damage, AFD

### 1.6.1 Formulation of AFD

To gain insight into EM failure, a governing parameter for EM damage in metal lines has been identified [1]. The parameter governing EM damage was formulated

on the basis of the divergence of the atomic flux induced by EM, and is denoted as *AFD*. An *AFD*-based method for predicting EM failure has been developed; this method allows the lifetime and possible failure site to be predicted accurately and universally.

The prediction of EM failure, that is, estimating the lifetime and failure location, has been attempted by using an empirical equation [6] and numerical simulations [40, 45, 46]. On the other hand, the evaluation of the threshold current density is also of great interest. The threshold value has conventionally been evaluated under the assumption that the product of the threshold and line length is constant [8, 47]. The predictions of lifetime and failure site, and the evaluation of  $j_{th}$  have been attempted separately in various works. With the introduction of the governing parameter for EM damage, *AFD*, the predictions and the evaluation can be carried out in a unified manner [1].

Formulations of *AFD* are considered for unpassivated polycrystalline lines, passivated polycrystalline lines, unpassivated bamboo lines and passivated bamboo lines, respectively. Metallic micro/nano structures can be fabricated by using EM in a polycrystalline line. Because the EM behavior in the passivated line includes the atomic density gradient in the specimen as described in Sect. 1.5, the formulation of *AFD* is more complex for passivated lines than unpassivated lines. The formulation of *AFD* for an unpassivated polycrystalline line is presented here to illustrate the fundamental concepts underlying *AFD*.

It can be assumed that metal atoms migrate along grain boundaries in a polycrystalline line. A model of the polycrystalline structure [57] is shown in Fig. 3, where  $d$  is the grain size. The thin metal lines have columnar grain structure. In this model, only one grain is assumed to be in the direction of line thickness. Let us consider the divergence of the atomic flux in the unit region enclosed by the rectangle in Fig. 3. The rectangle includes one triple point of grain boundaries with length  $l [= \sqrt{3}d/6]$ . Here,  $\Delta\phi$  is a constant related to the relative angle between grain boundaries, and  $\theta$  is the angle between Grain boundary-I and the  $x$ -axis of the Cartesian coordinate system ( $x$ ,  $y$ ). The  $x$  and  $y$  components of the current density vector and the temperature at the triple point are denoted by  $j_x$ ,  $j_y$  and  $T$ , respectively. Substituting the current density component along the grain boundary and the temperature at the end of each grain boundary into the Huntington–Grone equation (10), the atomic flux is obtained for the three points on the side of the rectangle. The sign of the flux is defined as positive for the direction outward from the unit region. After multiplying the effective width of the grain boundary  $\delta$  and the unit thickness by every atomic flux at the ends of Grain boundary-I, -II and -III, the number of atoms migrating along the grain boundaries per unit time is summed. The sum is divided by the volume of the unit region,  $A [= \sqrt{3}d^2/4]$ .

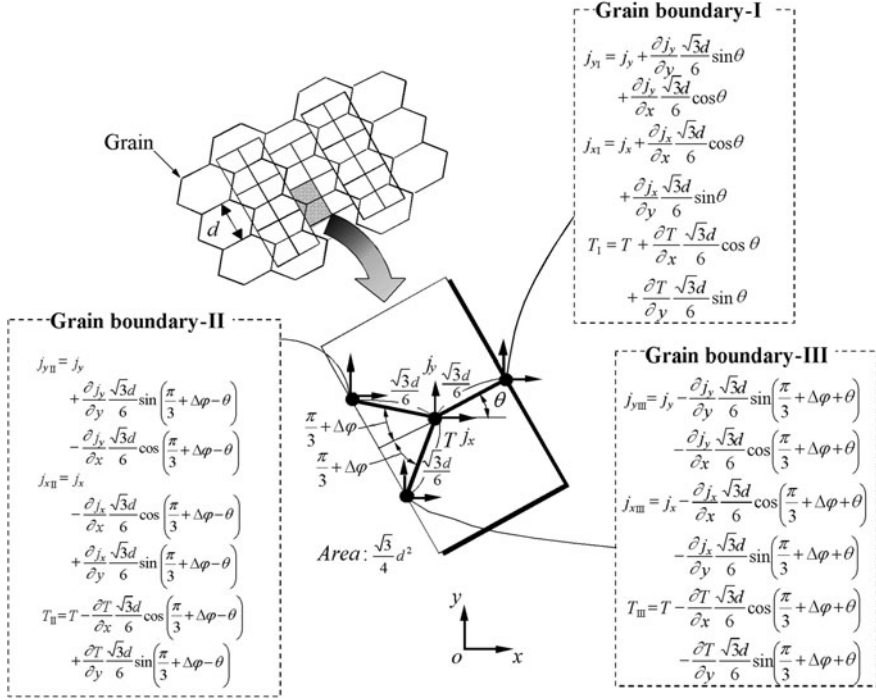


**Fig. 3** Model of polycrystalline structure

Thus, the divergence of the atomic flux in the unpassivated polycrystalline line  $AFD_{gb\theta}$  is formulated as follows:

$$AFD_{gb\theta} = \frac{(J_I + J_{II} + J_{III})\delta}{A}$$

$$= \frac{C_{gb}\rho\delta}{A} \left\{ \frac{1}{T_I} \exp\left(-\frac{Q_{gb}}{kT_I}\right) j_{I1}^* + \frac{1}{T_{II}} \exp\left(-\frac{Q_{gb}}{kT_{II}}\right) j_{II1}^* + \frac{1}{T_{III}} \exp\left(-\frac{Q_{gb}}{kT_{III}}\right) j_{III1}^* \right\}, \quad (12)$$

where  $J_I$ ,  $J_{II}$  and  $J_{III}$  are atomic fluxes,  $T_I$ ,  $T_{II}$  and  $T_{III}$  are temperatures, and  $j_{I1}^*$ ,  $j_{II1}^*$  and  $j_{III1}^*$  are components of the current density along the grain boundary, defining outward as positive, at the end of each Grain boundary-I, -II and -III. The activation energy for grain boundary diffusion is denoted as  $Q_{gb}$ , and the constant  $C_{gb}$  is given by

$$C_{gb} = \frac{ND_0eZ^*}{k}. \quad (13)$$

The atomic flux along each grain boundary at its end is calculated using each projection of current density components  $(j_{xI}, j_{yI})$ ,  $(j_{xII}, j_{yII})$  and  $(j_{xIII}, j_{yIII})$ , illustrated in Fig. 3, along the grain boundary for evaluating  $j_{I1}^*$ ,  $j_{II1}^*$  and  $j_{III1}^*$  in Eq. (12).

After that, we define  $\pi/3 + \Delta\varphi - \theta$  as  $\varphi_1$  and  $\pi/3 + \Delta\varphi + \theta$  as  $\varphi_2$ . By using the Maclaurin series with natural number  $n$ ,  $AFD_{\text{gb}\theta}$  is transformed as follows:

$$\begin{aligned}
 AFD_{\text{gb}\theta} = & \frac{C_{\text{gb}}\rho\delta}{A} \left\langle \frac{1}{T} \exp\left(-\frac{Q_{\text{gb}}}{kT}\right) \cos \theta \cdot \{1 - ()_{\text{I}}\} \right. \\
 & \times \left[ 1 + \frac{Q_{\text{gb}}}{kT}()_{\text{I}} + \frac{1}{2} \left\{ \frac{Q_{\text{gb}}}{kT}()_{\text{I}} \right\}^2 + \cdots + \frac{1}{n!} \left\{ \frac{Q_{\text{gb}}}{kT}()_{\text{I}} \right\}^n \right] (j_x + X_{\text{jxl}}) \\
 & + \frac{1}{T} \exp\left(-\frac{Q_{\text{gb}}}{kT}\right) \sin \theta \cdot \{1 - ()_{\text{I}}\} \\
 & \times \left[ 1 + \frac{Q_{\text{gb}}}{kT}()_{\text{I}} + \frac{1}{2} \left\{ \frac{Q_{\text{gb}}}{kT}()_{\text{I}} \right\}^2 + \cdots + \frac{1}{n!} \left\{ \frac{Q_{\text{gb}}}{kT}()_{\text{I}} \right\}^n \right] (j_y + X_{\text{jyl}}) \\
 & + \frac{1}{T} \exp\left(-\frac{Q_{\text{gb}}}{kT}\right) (-\cos \varphi_1) \cdot \{1 - ()_{\text{II}}\} \\
 & \times \left[ 1 + \frac{Q_{\text{gb}}}{kT}()_{\text{II}} + \frac{1}{2} \left\{ \frac{Q_{\text{gb}}}{kT}()_{\text{II}} \right\}^2 + \cdots + \frac{1}{n!} \left\{ \frac{Q_{\text{gb}}}{kT}()_{\text{II}} \right\}^n \right] (j_x + X_{\text{jxl}}) \\
 & + \frac{1}{T} \exp\left(-\frac{Q_{\text{gb}}}{kT}\right) \sin \varphi_1 \cdot \{1 - ()_{\text{II}}\} \\
 & \times \left[ 1 + \frac{Q_{\text{gb}}}{kT}()_{\text{II}} + \frac{1}{2} \left\{ \frac{Q_{\text{gb}}}{kT}()_{\text{II}} \right\}^2 + \cdots + \frac{1}{n!} \left\{ \frac{Q_{\text{gb}}}{kT}()_{\text{II}} \right\}^n \right] (j_y + X_{\text{jyl}}) \\
 & + \frac{1}{T} \exp\left(-\frac{Q_{\text{gb}}}{kT}\right) (-\cos \varphi_2) \cdot \{1 - ()_{\text{III}}\} \\
 & \times \left[ 1 + \frac{Q_{\text{gb}}}{kT}()_{\text{III}} + \frac{1}{2} \left\{ \frac{Q_{\text{gb}}}{kT}()_{\text{III}} \right\}^2 + \cdots + \frac{1}{n!} \left\{ \frac{Q_{\text{gb}}}{kT}()_{\text{III}} \right\}^n \right] (j_x + X_{\text{jxl}}) \\
 & + \frac{1}{T} \exp\left(-\frac{Q_{\text{gb}}}{kT}\right) (-\sin \varphi_2) \cdot \{1 - ()_{\text{III}}\} \\
 & \times \left[ 1 + \frac{Q_{\text{gb}}}{kT}()_{\text{III}} + \frac{1}{2} \left\{ \frac{Q_{\text{gb}}}{kT}()_{\text{III}} \right\}^2 + \cdots + \frac{1}{n!} \left\{ \frac{Q_{\text{gb}}}{kT}()_{\text{III}} \right\}^n \right] (j_y + X_{\text{jyl}}) \Bigg\rangle,
 \end{aligned} \tag{14}$$

where

$$()_{\text{I}} = X_{\text{Tl}} - X_{\text{Tl}}^2 + \cdots + (-1)^{r+1} X_{\text{Tl}}^r + \cdots, \tag{15}$$

$$X_{\text{Tl}} = \frac{\frac{\partial T}{\partial x} l \cos \theta + \frac{\partial T}{\partial y} l \sin \theta}{T}, \tag{16}$$

$$X_{\text{jxl}} = \frac{\partial j_x}{\partial x} l \cos \theta + \frac{\partial j_x}{\partial y} l \sin \theta, \tag{17}$$



$$X_{j_{yI}} = \frac{\partial j_y}{\partial x} l \cos \theta + \frac{\partial j_y}{\partial y} l \sin \theta, \quad (18)$$

$$()_{II} = X_{T_{II}} - X_{T_{II}}^2 + \dots + (-1)^{r+1} X_{T_{II}}^r + \dots, \quad (19)$$

$$X_{T_{II}} = \frac{-\frac{\partial T}{\partial x} l \cos \varphi_1 + \frac{\partial T}{\partial y} l \sin \varphi_1}{T}, \quad (20)$$

$$X_{j_{xII}} = -\frac{\partial j_x}{\partial x} l \cos \varphi_1 + \frac{\partial j_x}{\partial y} l \sin \varphi_1, \quad (21)$$

$$X_{j_{yII}} = -\frac{\partial j_y}{\partial x} l \cos \varphi_1 + \frac{\partial j_y}{\partial y} l \sin \varphi_1, \quad (22)$$

$$()_{III} = X_{T_{III}} - X_{T_{III}}^2 + \dots + (-1)^{r+1} X_{T_{III}}^r + \dots, \quad (23)$$

$$X_{T_{III}} = \frac{-\frac{\partial T}{\partial x} l \cos \varphi_2 - \frac{\partial T}{\partial y} l \sin \varphi_2}{T}, \quad (24)$$

$$X_{j_{xIII}} = -\frac{\partial j_x}{\partial x} l \cos \varphi_2 - \frac{\partial j_x}{\partial y} l \sin \varphi_2, \quad (25)$$

and

$$X_{j_{yIII}} = -\frac{\partial j_y}{\partial x} l \cos \varphi_2 - \frac{\partial j_y}{\partial y} l \sin \varphi_2. \quad (26)$$

As discussed later, the following relation holds:

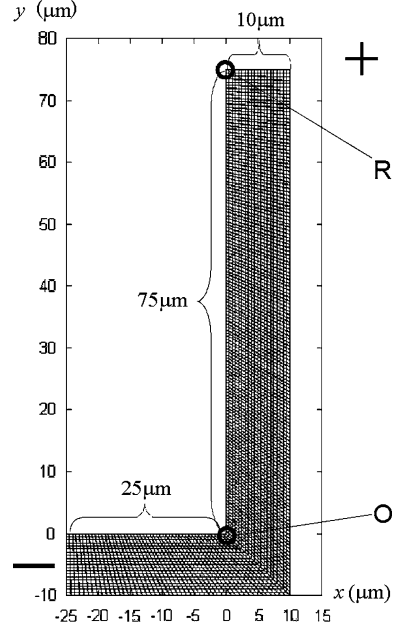
$$|X_{T_I}|, |X_{T_{II}}|, |X_{T_{III}}| \leq 1. \quad (27)$$

Each term in angle brackets  $\langle \rangle$  in Eq. (14) is composed of the product of the curly brackets  $\{ \}$  and square brackets  $[ ]$ , both of which include a term of 1. We can calculate the values of the terms in each set of brackets and eliminate small terms.

### 1.6.2 Comparison of Terms in AFD Formula

There is no need to consider all terms in Eq. (14) in a general operation environment, and some small terms can be neglected. The value of each term is estimated under a general condition in the acceleration test of EM, that is, input current density  $j_\infty = 0.1\text{--}3.0 \text{ MA/cm}^2$ , substrate temperature  $T_s = 373\text{--}676 \text{ K}$ , grain size  $d = 0.4\text{--}0.8 \text{ }\mu\text{m}$  and activation energy  $Q_{gb} = 0.567 \text{ eV}$  [58]. The AFD values are calculated assuming the line shape shown in Fig. 4. The Cartesian coordinate system  $(x, y)$  shown in Fig. 4 is used. In the assessment of small terms, the metal line with a single bend between the current input/output, such as contact pads or vias is treated. In the angled metal line, the electric current distribution and

**Fig. 4** Model of asymmetrically angled line



temperature distribution in the straight part differ from those near the corner, and the values of terms in the *AFD* expression differ between the straight part and the corner. The current density is known to be concentrated near the corner and the temperature gradient is very large near the corner of an asymmetrically angled line [56]. Therefore, the values of the terms in Eq. (14) are estimated in each straight part, R, and in the corner, O, in Fig. 4. Current distribution and the temperature distribution in each part are calculated by utilizing finite element (FE) analysis based on the governing equation given below.

Taking electrical potential as  $\phi_e$ , the governing equation for electrical potential is given by

$$\nabla^2 \phi_e = 0, \quad (28)$$

where  $\nabla^2 = \partial^2/\partial x^2 + \partial^2/\partial y^2$ . Ohm's law is written as

$$\mathbf{j} = -\frac{1}{\rho_0} \text{grad} \phi_e. \quad (29)$$

The equation of steady-state heat conduction is

$$\lambda \nabla^2 T + \rho_0 \mathbf{j} \cdot \mathbf{j} = 0, \quad (30)$$

where  $\lambda$  is the thermal conductivity. The quantities of  $\lambda$  and  $\rho_0$  are assumed to be 0.000233 W/(μm K) and 0.0445 Ω μm [58].

The line shown in Fig. 4 is asymmetrically angled at a higher ratio (25:75) in comparison with a line generally used for acceleration tests [29, 32]. This higher ratio leads to a higher temperature gradient near the corner. Note that here we consider the metal line bent only once between the current input and output. Although heat actually flows from the line to its surroundings [57], this heat flow is not taken into account in Eq. (30); consequently, the highest possible peak temperature is estimated over the limited line length. Thus, the above model can estimate the largest possible temperature gradient not only near the corner, O, but also at the end of the straight part, R.

When input current density  $j_\infty$  becomes large, terms related to the current density gradient at point O (e.g.,  $X_{j_{xl}}$  and  $X_{j_{yl}}$ ), and terms related to the temperature gradient at points R and O (e.g.,  $X_{T_l}$ ), also become large. When substrate temperature  $T_s$  becomes small, terms related to the temperature gradient become large. Accordingly, we assume that  $j_\infty$  is larger and  $T_s$  is smaller for the boundary conditions of the FE analysis, in order to compare the magnitude of terms under the largest possible estimation. Then, we performed FE analysis under boundary conditions of  $j_\infty = 3 \text{ MA/cm}^2$  and  $T_s = 373 \text{ K}$ .

### 1.6.3 Comparison in Straight Part of Angled Metal Line

Let us derive the *AFD* formula for the straight part in the model discussed in Sect. 1.6.2. Each term in the formula should be estimated to be as large as possible. A numerator of the fraction  $X_{T_l}$  takes the largest value at point R when the direction of Grain boundary-I coincides with longitudinal direction of the line (i.e.,  $\theta = \pi/2$ ) because the temperature gradient is greatest along the longitudinal direction of the line (i.e., along the y-axis). Thus, the term for temperature gradient,  $X_{T_l}$ , has the following relation:

$$X_{T_l} = \frac{\frac{\partial T}{\partial x} l \cos \theta + \frac{\partial T}{\partial y} l \sin \theta}{T} \leq \frac{\left| \frac{\partial T}{\partial y} \right| l}{T}. \quad (\text{at point R}) \quad (31)$$

Then, the quantity of  $X_{T_l}$  is calculated by using the most right-hand side of Eq. (31) to obtain the largest possible estimate. When the grain size  $d$  becomes large, the term  $X_{T_l}$  proportionally becomes large because of increasing  $l [= \sqrt{3}d/6]$ . The grain size  $d$  is 0.4–0.8  $\mu\text{m}$  for general Al lines. We assume that  $d = 0.8 \mu\text{m}$  and  $l = 0.231 \mu\text{m}$  to obtain the largest possible estimate of  $X_{T_l}$ . The values of each term in the first term of the angle brackets  $\langle \rangle$  in Eq. (14) are calculated by using FE analysis results for current density, temperature and temperature gradient (9.05 K/ $\mu\text{m}$ ) at point R in Fig. 4:

$$X_{T_l} = 0.00560,$$

$$X_{j_{xl}} = 0$$

and

$$\frac{Q_{\text{gb}}}{kT}X_{T_1} = 0.0988.$$

Considering the above values, the term  $X_{T_1}^2$  and higher-order terms included in curly brackets  $\{1 - (\ )_I\}$  in Eq. (14) are much smaller than 1. Here, we neglect the terms smaller than 0.005. The relation  $Q_{\text{gb}}(\ )_I/(kT) \approx Q_{\text{gb}}X_{T_1}/(kT)$  holds, and the term of  $1/2\{Q_{\text{gb}}(\ )_I/(kT)\}^2$  and higher-order terms are removed from the square brackets  $[\ ]$  in Eq. (14). There is no need to consider  $X_{j_{\text{xl}}}$  in parentheses  $(j_x + X_{j_{\text{xl}}})$  in Eq. (14) because the current density gradient is zero in the straight part. To preserve an arbitrariness of setting of coordinate system,  $j_x$  should remain in the parentheses although the value of  $J_x$  vanishes at point R.

After the elimination of negligible terms, the curly brackets  $\{ \}$  and square brackets  $[ \ ]$  in Eq. (14) are expanded. Then, terms smaller than 0.005 are omitted. The negligible term is as follows:

$$\frac{Q_{\text{gb}}}{kT}X_{T_1} \times X_{T_1} = 0.000554.$$

In this way, small terms are erased in the first term in angle brackets  $\langle \rangle$  in Eq. (14). As for the other terms in the angle brackets  $\langle \rangle$ , small terms are also eliminated and the curly brackets  $\{ \}$  and square brackets  $[ \ ]$  are expanded in a similar manner. We next obtain the *AFD* formula for the straight part R as follows:

$$\begin{aligned} AFD_{\text{gb}\theta} = & \frac{C_{\text{gb}}\rho\delta}{A} \frac{1}{T} \exp\left(-\frac{Q_{\text{gb}}}{kT}\right) \\ & \times \left[ j_x(\cos\theta - \cos\varphi_1 - \cos\varphi_2) + j_y(\sin\theta + \sin\varphi_1 - \sin\varphi_2) \right. \\ & + \frac{1}{T} \left( \frac{Q_{\text{gb}}}{kT} \right) \left\{ \frac{\partial T}{\partial x} j_x l (\cos^2\theta + \cos^2\varphi_1 + \cos^2\varphi_2) \right. \\ & + \frac{\partial T}{\partial y} j_y l (\sin^2\theta + \sin^2\varphi_1 + \sin^2\varphi_2) \\ & \left. \left. + \left( \frac{\partial T}{\partial x} j_y + \frac{\partial T}{\partial y} j_x \right) l (\sin\theta \cos\theta - \sin\varphi_1 \cos\varphi_1 + \sin\varphi_2 \cos\varphi_2) \right\} \right]. \end{aligned} \quad (32)$$

Then, we expand the trigonometric functions including  $\varphi_1 [= \pi/3 + \Delta\varphi - \theta]$  and  $\varphi_2 [= \pi/3 + \Delta\varphi + \theta]$  with a minimal angle of  $\Delta\varphi$   $[=-0.0236 \text{ rad}]$  [59] by using the Maclaurin series and remove terms smaller than 0.005 in

comparison with 1. The *AFD* formula for the straight part is transformed as follows:

$$AFD_{gb\theta} = C_{gb}\rho\delta\frac{4}{\sqrt{3}d^2}\frac{1}{T}\exp\left(-\frac{Q_{gb}}{kT}\right)\left[\sqrt{3}\Delta\varphi(j_x\cos\theta + j_y\sin\theta) + \frac{\sqrt{3}d}{4T}\left(\frac{Q_{gb}}{kT}\right)\left(\frac{\partial T}{\partial x}j_x + \frac{\partial T}{\partial y}j_y\right) - \frac{\sqrt{3}d}{4T}\left(\frac{\partial T}{\partial x}j_x + \frac{\partial T}{\partial y}j_y\right)\right], \quad (33)$$

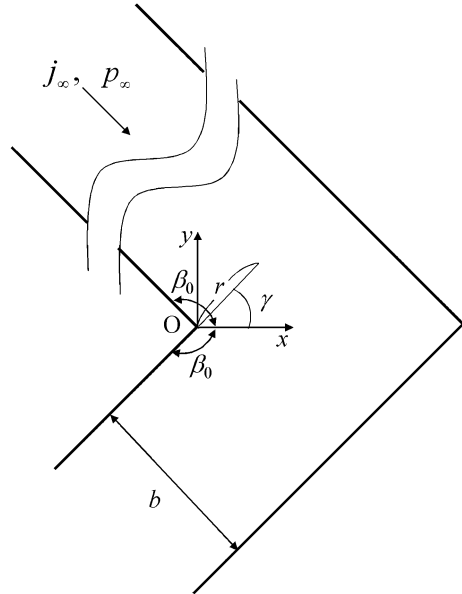
### 1.6.4 Comparison Near Corner of Angled Metal Line

The current and temperature distributions near the corner of the angled metal line shown in Fig. 5 are expressed by asymptotic solutions [56]. Cartesian coordinates ( $x$ ,  $y$ ) and polar coordinates ( $r$ ,  $\gamma$ ) are shown in Fig. 5. The line width is  $b$ , the corner angle is  $2\beta_0$  and the input current density is  $j_\infty$ . Then, the values of current density, its gradient and temperature gradient are obtained by using the following asymptotic solutions accompanied with the results of FE analysis to compare the terms in Eq. (14) near the corner:

$$j_x = -K_e\left(\frac{r}{b}\right)^{\frac{\pi}{2\beta_0}-1}\sin\left(\frac{\pi}{2\beta_0}-1\right)\gamma, \quad (34)$$

$$j_y = -K_e\left(\frac{r}{b}\right)^{\frac{\pi}{2\beta_0}-1}\cos\left(\frac{\pi}{2\beta_0}-1\right)\gamma, \quad (35)$$

**Fig. 5** Infinite metal line



$$\frac{\partial j_x}{\partial x} = -\frac{\partial j_y}{\partial y} = K_e \left( \frac{\pi}{2\beta_0} - 1 \right) \frac{1}{b} \left( \frac{r}{b} \right)^{\frac{\pi}{2\beta_0}-2} \sin \left( \frac{\pi}{2\beta_0} - 2 \right) \gamma, \quad (36)$$

$$\frac{\partial j_x}{\partial y} = \frac{\partial j_y}{\partial x} = -K_e \left( \frac{\pi}{2\beta_0} - 1 \right) \frac{1}{b} \left( \frac{r}{b} \right)^{\frac{\pi}{2\beta_0}-2} \cos \left( \frac{\pi}{2\beta_0} - 2 \right) \gamma, \quad (37)$$

$$\frac{\partial T}{\partial x} = \frac{1}{\lambda} K_t \left( \frac{r}{b} \right)^{\frac{\pi}{2\beta_0}-1} \sin \left( \frac{\pi}{2\beta_0} - 1 \right) \gamma \quad (38)$$

and

$$\frac{\partial T}{\partial y} = \frac{1}{\lambda} K_t \left( \frac{r}{b} \right)^{\frac{\pi}{2\beta_0}-1} \cos \left( \frac{\pi}{2\beta_0} - 1 \right) \gamma, \quad (39)$$

where  $K_e = \beta_0^{\pi/2\beta_0-1} j_\infty$ ,  $K_t = \beta_0^{\pi/2\beta_0-1} p_\infty$ , and  $p_\infty$  is the heat flux considering Joule heating far from the corner, which is expressed by

$$p_\infty = q_R + \phi_R j_\infty. \quad (40)$$

Here,  $q_R$  and  $\phi_R$  are the heat flux and electrical potential at point R far from the corner, as shown in Fig. 4.  $\phi_R$  is taken at point R when the electrical potential is zero at the inner corner.

In essence,  $p_\infty$  represents the heat flux induced by the temperature difference between the two points far from the corner, which are symmetric to each other around the bisector of the corner. The temperature difference between the symmetric points originates from the Joule heating generated in the lines around the angle line and/or in the asymmetrically angled line itself. One can directly measure the heat flux  $q_R$ , which includes the heat flux induced by the temperature difference between the symmetric points  $p_\infty$  and the heat flux due to Joule heating generated symmetrically around the bisector [56]. If the electric current is turned off to eliminate the heat flux by symmetric Joule heating from  $q_R$ , the temperature difference between the symmetric points also vanishes because this temperature difference originates from Joule heating. The heat flux  $p_\infty$ , therefore, cannot be measured separately, but can be extracted from  $q_R$  by using Eq. (40). Since the heat flux  $p_\infty$  originates from Joule heating, the solutions given by Eqs. (38) and (39) are effective under the flow of electric current.

The current density, its gradient and temperature gradient near the corner in the model described in Sect. 1.6.2 are estimated using Eqs. (34)–(39). The AFD formula near the corner is derived using these values.

Now, let us consider the region at  $r = d$  as a corner part. The grain size  $d$  is 0.4–0.8  $\mu\text{m}$  for a typical Al lines. When the grain size becomes small, the term  $X_{T_1}$  near the corner becomes large because of a singularity of temperature gradient at the corner vertex. Each term to be compared should be estimated to be as large as possible. Accordingly, it is assumed that  $d = 0.4 \mu\text{m}$  and  $l = 0.115 \mu\text{m}$ . The heat flux  $q_R$  and electrical potential  $\phi_R$  at R are calculated by

FE analysis, and thereby we obtain the value of  $p_\infty$ . Equations (34)–(39) also yield the following relation:

$$|j_x| = \left| -K_e \left( \frac{r}{b} \right)^{\frac{\pi}{2\beta_0}-1} \sin \left( \frac{\pi}{2\beta_0} - 1 \right) \gamma \right| \leq \left| K_e \left( \frac{r}{b} \right)^{\frac{\pi}{2\beta_0}-1} \right|. \quad (41)$$

Similarly,

$$|j_y| \leq \left| K_e \left( \frac{r}{b} \right)^{\frac{\pi}{2\beta_0}-1} \right|, \quad (42)$$

$$\left| \frac{\partial j_x}{\partial x} \right|, \left| \frac{\partial j_y}{\partial y} \right|, \left| \frac{\partial j_x}{\partial y} \right|, \left| \frac{\partial j_y}{\partial x} \right| \leq \left| K_e \left( \frac{\pi}{2\beta_0} - 1 \right) \frac{1}{b} \left( \frac{r}{b} \right)^{\frac{\pi}{2\beta_0}-2} \right| \quad (43)$$

and

$$\left| \frac{\partial T}{\partial x} \right|, \left| \frac{\partial T}{\partial y} \right| \leq \left| \frac{1}{\lambda} K_t \left( \frac{r}{b} \right)^{\frac{\pi}{2\beta_0}-1} \right|. \quad (44)$$

The values of current density, its gradient and temperature gradient can be calculated using the most right-hand sides of Eqs. (41)–(44) to obtain the largest possible estimates.

Regarding the term  $X_{T_1}$  in the first term of angle brackets  $\langle \rangle$  in Eq. (14), in order to find the largest possible temperature gradient independent of the coordinate setting,  $\partial T/\partial x = \partial T/\partial y$  is assumed. By obtaining the extremum of the numerator with respect to  $\theta$ , the term concerning the temperature gradient,  $X_{T_1}$ , has the following relation:

$$X_{T_1} = \frac{\frac{\partial T}{\partial x} l \cos \theta + \frac{\partial T}{\partial y} l \sin \theta}{T} \leq \frac{\sqrt{2} \left| \frac{\partial T}{\partial x} \right| l}{T} \quad (\text{at point O}). \quad (45)$$

Then, the value of  $X_{T_1}$  is calculated using the most right-hand side of Eq. (45) to obtain the largest possible estimate. Using Eqs. (44) and (45), the following values are obtained:

$$X_{T_1} = 0.00277$$

and

$$\frac{Q_{gb}}{kT} X_{T_1} = 0.0326,$$

where the angle  $\beta_0 = 3\pi/4$  and the values  $p_\infty = 0.00101 \text{ W}/(\mu\text{m K})$  and  $T = 559 \text{ K}$  obtained by FE analysis are used.

Thus, the term  $X_{T_1}$  and higher-order terms included in curly brackets  $\{1 - (\cdot)_1\}$  in Eq. (14) are negligible because these terms are smaller than 0.005. Moreover, the relation  $Q_{gb}(\cdot)_1/(kT) \approx Q_{gb}X_{T_1}/(kT)$  holds, and the term  $1/2\{Q_{gb}(\cdot)_1/(kT)\}^2$  and higher-order terms are omitted in the square brackets  $[\cdot]$  in Eq. (14).

As for the parentheses  $(j_x + X_{jxl})$  in Eq. (14), the current density and its gradient are estimated to be as large as possible using the relations Eqs. (41)–(43). Then, the parentheses  $(j_x + X_{jxl})$  in the first term of the angle brackets  $\langle \rangle$  in Eq. (14) is written as

$$(j_x + X_{jxl}) = j_x \left( 1 + \frac{X_{jxl}}{j_x} \right). \quad (46)$$

If the quantity  $X_{jxl}$  is maximized in the evaluation, the following relation is obtained in the same manner as Eq. (45):

$$\frac{X_{jxl}}{j_x} = \frac{\frac{\partial j_x}{\partial x} l \cos \theta + \frac{\partial j_x}{\partial y} l \sin \theta}{j_x} \leq \frac{\sqrt{2} \left| \frac{\partial j_x}{\partial x} \right| l}{|j_x|} \quad (\text{at point O}). \quad (47)$$

Note that the value of  $j_x$  should be maximized. The quantity  $X_{jxl}/j_x$  is calculated using the most right-hand side of Eq. (47). The value is obtained as

$$\frac{X_{jxl}}{j_x} = \frac{\sqrt{2} l}{r} \left| \frac{\pi}{2\beta_0} - 1 \right| = 0.136.$$

This value is greater than 0.005; thus, the term  $X_{jxl}/j_x$  remains in the parentheses () on the right-hand side of Eq. (46).

After eliminating negligible terms, the curly brackets  $\{ \}$ , square brackets  $[ ]$  and parentheses  $( )$  concerning current density in Eq. (14) are expanded. Then, terms smaller than 0.005 are omitted. A negligible term is as follows:

$$\frac{Q_{gb}}{kT} X_{T_1} \times \frac{X_{jxl}}{j_x} = 0.00442$$

In the first term in the angle brackets  $\langle \rangle$  in Eq. (14), small terms are omitted. As for other terms in angle brackets  $\langle \rangle$ , negligible terms are also eliminated and the braces are expanded in a similar manner. Then, one can obtain the following *AFD* formula for the corner part, O:

$$\begin{aligned} AFD_{gb\theta} &= \frac{C_{gb}\rho\delta}{A} \frac{1}{T} \exp\left(-\frac{Q_{gb}}{kT}\right) \\ &\times \left[ j_x(\cos \theta - \cos \varphi_1 - \cos \varphi_2) + j_y(\sin \theta + \sin \varphi_1 - \sin \varphi_2) \right. \\ &+ \frac{\partial j_x}{\partial x} l(\cos^2 \theta + \cos^2 \varphi_1 + \cos^2 \varphi_2) + \frac{\partial j_y}{\partial y} l(\sin^2 \theta + \sin^2 \varphi_1 + \sin^2 \varphi_2) \\ &+ \left( \frac{\partial j_x}{\partial y} + \frac{\partial j_y}{\partial x} \right) l(\sin \theta \cos \theta - \sin \varphi_1 \cos \varphi_1 + \sin \varphi_2 \cos \varphi_2) \\ &\left. + \frac{1}{T} \left( \frac{Q_{gb}}{kT} \right) \left\{ \frac{\partial T}{\partial x} j_x l(\cos^2 \theta + \cos^2 \varphi_1 + \cos^2 \varphi_2) \right. \right. \end{aligned}$$



$$\begin{aligned}
& + \frac{\partial T}{\partial y} j_y l (\sin^2 \theta + \sin^2 \varphi_1 + \sin^2 \varphi_2) \\
& + \left( \frac{\partial T}{\partial x} j_y + \frac{\partial T}{\partial y} j_x \right) l (\sin \theta \cos \theta - \sin \varphi_1 \cos \varphi_1 + \sin \varphi_2 \cos \varphi_2) \Bigg\} \Bigg].
\end{aligned} \tag{48}$$

Now, let us expand the trigonometric functions including  $\varphi_1$  and  $\varphi_2$  with a minimal angle  $\Delta\varphi$  by using the Maclaurin series and omit terms smaller than 0.005. The *AFD* formula for the corner part is transformed as follows:

$$\begin{aligned}
AFD_{gb\theta} = C_{gb} \rho \delta \frac{4}{\sqrt{3}d^2} \frac{1}{T} \exp\left(-\frac{Q_{gb}}{kT}\right) & \left[ \sqrt{3} \Delta\varphi (j_x \cos \theta + j_y \sin \theta) \right. \\
& - \frac{d}{2} \Delta\varphi \left\{ \left( \frac{\partial j_x}{\partial x} - \frac{\partial j_y}{\partial y} \right) \cos 2\theta + \left( \frac{\partial j_x}{\partial y} + \frac{\partial j_y}{\partial x} \right) \sin 2\theta \right\} \\
& \left. + \frac{\sqrt{3}d}{4T} \left( \frac{Q_{gb}}{kT} \right) \left( \frac{\partial T}{\partial x} j_x + \frac{\partial T}{\partial y} j_y \right) \right].
\end{aligned} \tag{49}$$

### 1.6.5 General Expression of *AFD*

To obtain the general expression of *AFD* that is applicable to both the straight part and the corner, the formula should include all terms in Eqs. (33) and (49). Thus, one can obtain a general expression of *AFD* [57] as

$$\begin{aligned}
AFD_{gb\theta} = C_{gb} \rho \delta \frac{4}{\sqrt{3}d^2} \frac{1}{T} \exp\left(-\frac{Q_{gb}}{kT}\right) & \left[ \sqrt{3} \Delta\varphi (j_x \cos \theta + j_y \sin \theta) \right. \\
& - \frac{d}{2} \Delta\varphi \left\{ \left( \frac{\partial j_x}{\partial x} - \frac{\partial j_y}{\partial y} \right) \cos 2\theta + \left( \frac{\partial j_x}{\partial y} + \frac{\partial j_y}{\partial x} \right) \sin 2\theta \right\} \\
& \left. + \frac{\sqrt{3}d}{4T} \left( \frac{Q_{gb}}{kT} - 1 \right) \left( \frac{\partial T}{\partial x} j_x + \frac{\partial T}{\partial y} j_y \right) \right].
\end{aligned} \tag{50}$$

It can be confirmed that the obtained formula of *AFD* is applicable not only to acceleration conditions but also to conditions with lower current density and higher substrate temperature.

### 1.6.6 Constant Electrical Resistivity within Rectangular Unit

Temperature may vary slightly within the rectangular unit shown in Fig. 3. Although the electrical resistivity depends on temperature, it was assumed that the electrical resistivity  $\rho$  in Eq. (12) was constant within the rectangular unit. Here the effect of the assumption in formulation of *AFD* is discussed. By explicitly

expressing the difference in  $\rho$  due to temperature distribution in the unit, Eq. (12) is transformed as follows:

$$\begin{aligned} AFD_{gb\theta} &= \frac{(J_I + J_{II} + J_{III})\delta}{A} \\ &= \frac{C_{gb}\delta}{A} \left\{ \frac{1}{T_I} \exp\left(-\frac{Q_{gb}}{kT_I}\right) \rho_{I1}^* + \frac{1}{T_{II}} \exp\left(-\frac{Q_{gb}}{kT_{II}}\right) \rho_{II1}^* + \frac{1}{T_{III}} \exp\left(-\frac{Q_{gb}}{kT_{III}}\right) \rho_{III1}^* \right\}, \end{aligned} \quad (51)$$

where the electrical resistivity at the end of Grain boundary-I, -II and -III in Fig. 3 is given by  $\rho_i [= \rho(1 + \alpha TX_{T_i})]$  ( $i = I, II, III$ ). Considering the derivation of  $AFD$  described above, one can obtain the following expression:

$$\begin{aligned} AFD_{gb\theta} &= \frac{C_{gb}\rho\delta}{A} \left\langle \frac{1}{T} \exp\left(-\frac{Q_{gb}}{kT}\right) \cos\theta \cdot \{1 - ()_I\} \right. \\ &\quad \times \left[ 1 + \frac{Q_{gb}}{kT} ()_I + \frac{1}{2} \left\{ \frac{Q_{gb}}{kT} ()_I \right\}^2 + \cdots + \frac{1}{n!} \left\{ \frac{Q_{gb}}{kT} ()_I \right\}^n \right] (j_x + X_{j_{xl}}) (1 + \alpha TX_{T_I}) \\ &\quad + \frac{1}{T} \exp\left(-\frac{Q_{gb}}{kT}\right) \sin\theta \cdot \{1 - ()_I\} \\ &\quad \times \left[ 1 + \frac{Q_{gb}}{kT} ()_I + \frac{1}{2} \left\{ \frac{Q_{gb}}{kT} ()_I \right\}^2 + \cdots + \frac{1}{n!} \left\{ \frac{Q_{gb}}{kT} ()_I \right\}^n \right] (j_y + X_{j_{yl}}) (1 + \alpha TX_{T_I}) \\ &\quad + \frac{1}{T} \exp\left(-\frac{Q_{gb}}{kT}\right) (-\cos\varphi_1) \cdot \{1 - ()_{II}\} \\ &\quad \times \left[ 1 + \frac{Q_{gb}}{kT} ()_{II} + \frac{1}{2} \left\{ \frac{Q_{gb}}{kT} ()_{II} \right\}^2 + \cdots + \frac{1}{n!} \left\{ \frac{Q_{gb}}{kT} ()_{II} \right\}^n \right] (j_x + X_{j_{xII}}) (1 + \alpha TX_{T_{II}}) \\ &\quad + \frac{1}{T} \exp\left(-\frac{Q_{gb}}{kT}\right) \sin\varphi_1 \cdot \{1 - ()_{II}\} \\ &\quad \times \left[ 1 + \frac{Q_{gb}}{kT} ()_{II} + \frac{1}{2} \left\{ \frac{Q_{gb}}{kT} ()_{II} \right\}^2 + \cdots + \frac{1}{n!} \left\{ \frac{Q_{gb}}{kT} ()_{II} \right\}^n \right] (j_y + X_{j_{yII}}) (1 + \alpha TX_{T_{II}}) \\ &\quad + \frac{1}{T} \exp\left(-\frac{Q_{gb}}{kT}\right) (-\cos\varphi_2) \cdot \{1 - ()_{III}\} \\ &\quad \times \left[ 1 + \frac{Q_{gb}}{kT} ()_{III} + \frac{1}{2} \left\{ \frac{Q_{gb}}{kT} ()_{III} \right\}^2 + \cdots + \frac{1}{n!} \left\{ \frac{Q_{gb}}{kT} ()_{III} \right\}^n \right] (j_x + X_{j_{xIII}}) (1 + \alpha TX_{T_{III}}) \\ &\quad + \frac{1}{T} \exp\left(-\frac{Q_{gb}}{kT}\right) (-\sin\varphi_2) \cdot \{1 - ()_{III}\} \\ &\quad \times \left[ 1 + \frac{Q_{gb}}{kT} ()_{III} + \frac{1}{2} \left\{ \frac{Q_{gb}}{kT} ()_{III} \right\}^2 + \cdots + \frac{1}{n!} \left\{ \frac{Q_{gb}}{kT} ()_{III} \right\}^n \right] (j_y + X_{j_{yIII}}) (1 + \alpha TX_{T_{III}}) \left. \right\rangle. \end{aligned} \quad (52)$$

Here,  $\alpha$  of Al takes a value of  $0.002 \text{ K}^{-1}$  at room temperature for an Al thin film [39, 67]. The value of  $\alpha$  for a thin film is smaller than that for the bulk material [53, 67]. The value of  $\alpha TX_{T_i}$  ( $i = \text{I, II, III}$ ) is compared with 1 in Eq. (52) using the value of  $\alpha$  being  $0.002 \text{ K}^{-1}$ . When the reference temperature increases as in an acceleration test,  $\alpha$  decreases. Thus, if the term  $\alpha TX_{T_i}$  can be omitted at room temperature, the term is negligible even at higher temperatures. Because the term concerning the temperature gradient in the straight part  $X_{T_i}$  is larger than that near the corner, as described in Sects. 1.6.3 and 1.6.4, the values of  $\alpha TX_{T_i}$  are calculated using the values of  $T$  and  $X_{T_i}$  in the straight part:

$$\alpha TX_{T_i} = 0.00418 < 0.005$$

Thus, the terms  $\alpha TX_{T_i}$  can be neglected in Eq. (52), and Eq. (14) is given. Therefore, the effect of temperature distribution in the rectangular unit on the electrical resistivity is unnecessary to consider, and  $\rho$  can be regarded constant within the unit in the formulation of  $AFD$ .

### 1.6.7 Application of $AFD$

The value of  $AFD_{\text{gb}\theta}$  changes with the angle  $\theta$  between the rectangle unit and the  $x$ -axis. To extract only the positive values of  $AFD_{\text{gb}\theta}$  considering void formation, the sum of the value of  $AFD_{\text{gb}\theta}$  and its absolute value is divided by two, and the expected value from the extracted positive values is obtained by considering the angle  $\theta$  from 0 to  $2\pi$ . On the other hand, extracting only the negative values of  $AFD_{\text{gb}\theta}$  gives the atomic flux divergence  $AFD_{\text{gen}}$  of hillock formation in the polycrystalline lines:

$$AFD_{\text{gen}} = \frac{1}{4\pi} \int_0^{2\pi} (AFD_{\text{gb}\theta} - |AFD_{\text{gb}\theta}|) d\theta. \quad (53)$$

Equation (53) can be applied to two-dimensional problem. For a one-dimensional problem such as a straight line, the  $AFD_{\text{gen}}$  of hillock formation is simply formulated by integrating  $AFD_{\text{gb}\theta}$  with respect to  $\theta$  [80]:

$$AFD_{\text{gen}} = \frac{C_{\text{gb}} \rho \delta}{\pi d^2 T} \exp\left(-\frac{Q_{\text{gb}}}{kT}\right) \left\{ \frac{d}{\lambda} \rho j_{\infty}^3 x \theta_1 \frac{1}{T} \left( \frac{Q_{\text{gb}}}{kT} - 1 \right) - 4\Delta \phi j_{\infty} \sin \theta_1 \right\}. \quad (54)$$

Here,  $\theta_1$  is the critical value of  $\theta$  and the coordinate  $x$  is set along the longitudinal of the line with the origin at the center of the strip.

When the governing parameter for EM damage in the line covered with a passivation layer is considered, the Huntington–Grone equation (10) is replaced with the atomic flux in a passivated metal line, as given by Eq. (11). Then, one can

calculate the parameter  $AFD_{\text{gb}\theta}^*$  in the same manner as for the unpassivated line [62]:

$$\begin{aligned}
 AFD_{\text{gb}\theta}^* = & C_{\text{gb}}^* N \frac{4}{\sqrt{3}d^2 T} \exp \left\{ -\frac{Q_{\text{gb}} + \kappa\Omega(N - N_{\text{T}})/N_0 - \sigma_{\text{T}}\Omega}{kT} \right\} \\
 & \times \left\langle \sqrt{3}\Delta\varphi \left\{ (j_x \cos \theta + j_y \sin \theta) Z^* e\rho - \frac{\kappa\Omega}{N_0} \left( \frac{\partial N}{\partial x} \cos \theta + \frac{\partial N}{\partial y} \sin \theta \right) \right\} \right. \\
 & - \frac{d}{2} \Delta\varphi \left\{ \left( \frac{\partial j_x}{\partial x} - \frac{\partial j_y}{\partial y} \right) Z^* e\rho \cos 2\theta - \frac{\kappa\Omega}{N_0} \left( \frac{\partial^2 N}{\partial x^2} - \frac{\partial^2 N}{\partial y^2} \right) \cos 2\theta \right. \\
 & + \left. \left( \frac{\partial j_x}{\partial y} + \frac{\partial j_y}{\partial x} \right) Z^* e\rho \sin 2\theta - 2 \frac{\kappa\Omega \partial^2 N}{N_0 \partial x \partial y} \sin 2\theta \right\} \\
 & - \frac{\sqrt{3}}{4} d \frac{\kappa\Omega}{N_0} \left( \frac{\partial^2 N}{\partial x^2} + \frac{\partial^2 N}{\partial y^2} \right) - \frac{\kappa\Omega/N_0}{kT} \\
 & \times \left[ \frac{\sqrt{3}}{4} d \left\{ Z^* e\rho \left( j_x \frac{\partial N}{\partial x} + j_y \frac{\partial N}{\partial y} \right) - \frac{\kappa\Omega}{N_0} \left( \frac{\partial N}{\partial x} \frac{\partial N}{\partial x} + \frac{\partial N}{\partial y} \frac{\partial N}{\partial y} \right) \right\} \right. \\
 & - \frac{d}{2} \Delta\varphi \left\{ Z^* e\rho \left( j_x \frac{\partial N}{\partial y} + j_y \frac{\partial N}{\partial x} \right) - 2 \frac{\kappa\Omega \partial N}{N_0 \partial x \partial y} \right\} \sin 2\theta \left. \right] \\
 & + \frac{\sqrt{3}d}{4T} \left\{ \frac{Q_{\text{gb}} + \kappa\Omega(N - N_{\text{T}})/N_0 - \sigma_{\text{T}}\Omega}{kT} - 1 \right\} \\
 & \times \left\{ Z^* e\rho \left( j_x \frac{\partial T}{\partial x} + j_y \frac{\partial T}{\partial y} \right) - \frac{\kappa\Omega}{N_0} \left( \frac{\partial N}{\partial x} \frac{\partial T}{\partial x} + \frac{\partial N}{\partial y} \frac{\partial T}{\partial y} \right) \right\} \Bigg\rangle,
 \end{aligned} \tag{55}$$

where  $C_{\text{gb}}^* = D_0 \delta / k$ .

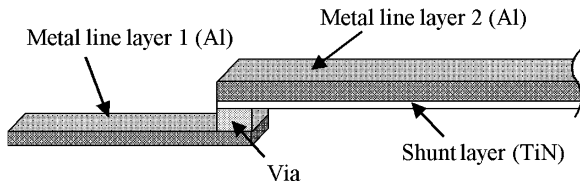
The governing parameter for EM damage in a passivated polycrystalline line,  $AFD_{\text{gen}}^*$ , is

$$AFD_{\text{gen}}^* = \frac{1}{4\pi} \int_0^{2\pi} \left( AFD_{\text{gb}\theta}^* - |AFD_{\text{gb}\theta}^*| \right) d\theta \quad (\text{for hillock formation}) \tag{56}$$

$$AFD_{\text{gen}}^* = \frac{1}{4\pi} \int_0^{2\pi} \left( AFD_{\text{gb}\theta}^* + |AFD_{\text{gb}\theta}^*| \right) d\theta \quad (\text{for void formation}). \tag{57}$$

The governing parameter  $AFD$  integrates all the factors that govern the damage, namely, the line structure, film characteristics, atomic density, as well as operating conditions such as current density and temperature. The parameter  $AFD$  gives the increase or decrease in the number of atoms per unit time and unit volume. By utilizing  $AFD$ , the distribution of atomic density  $N$  within the metal line can be calculated. Then, it is judged whether or not the atomic density is beyond a critical value for beginning void or hillock formation or for seeking the threshold current

**Fig. 6** Metal lines connected by via. Reprinted from Hasegawa et al. [31]. Copyright (2009) with permission from Elsevier



density [1]. An excess of atomic density over the critical value is used for reproducing the damage process until line failure, and lifetime and possible failure site are predicted [62].

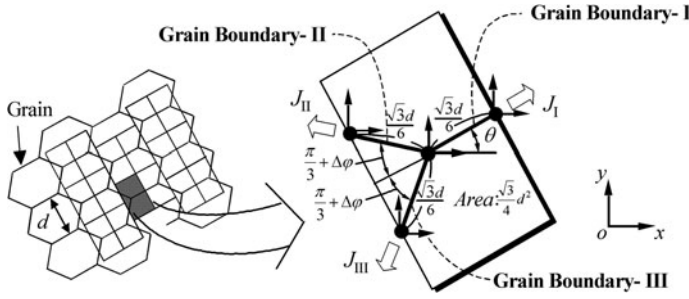
## 1.7 Derivation Method of Characteristic Constants of $EM^1$

### 1.7.1 Failure Mode in Via-Connected Line

The metal lines in IC are often connected by vias and multi-level interconnections are constructed. A schematic diagram of a typical interconnection with a via is shown in Fig. 6. The via for an Al interconnection is made of Al or tungsten (W). The metal lines are often stacked on a shunt layer made of refractory metal such as titanium nitride (TiN), by which the electric current can bypass the void formed in the Al line. In the metal line structure with a via, no Al atoms are supplied to the cathode end by EM because the line is not connected to a reservoir of the atoms such as pads and the atomic flow is intercepted by the via. Therefore, the metal line connected by the via has the failure mode whereby the cathode edge of the line drifts in the direction of electron flow as a result of EM [7]. A governing parameter for EM damage at the ends of a passivated polycrystalline line,  $AFD_{gen|end}^*$ , has been expressed by considering the boundary condition with respect to atomic diffusion [30], where no atoms flow into the cathode end or out of the anode end.

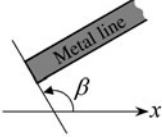
The method for deriving the EM characteristics of a metal line utilizes the EM-induced drift at the line end [31]. In this section the drift velocity induced at the line end by EM is theoretically expressed by using  $AFD_{gen|end}^*$ . By this derivation method, the film's characteristic constants in the formula of the parameter can be determined by measuring drift velocity. Next, the Al line modeled after the via-connected line is considered. The method based on  $AFD_{gen|end}^*$  is applied to two types of Al polycrystalline lines with different line lengths, and the values of drift velocity in such lines are experimentally measured. By equating the theoretical drift velocity with the experimental value, characteristic constants of the film are obtained. The method based on  $AFD_{gen|end}^*$  is able to approximate the constants.

<sup>1</sup> The contents concerning this section have been permitted to reprint from Hasegawa et al. [31], copyright (2009), with permission from Elsevier.



**Fig. 7** Model of polycrystalline microstructure. Reprinted from Hasegawa et al. [31]. Copyright (2009) with permission from Elsevier

**Table 1** Boundary conditions for atomic diffusion

Range-I	Range-II	Range-III	
$-2\pi/3 + \Delta\phi + \beta < \theta \leq -\pi/3 - \Delta\phi + \beta$	$-\pi/3 - \Delta\phi + \beta < \theta \leq \beta$	$\beta < \theta \leq \pi/3 + \Delta\phi + \beta$	
$J_{II} = J_{III} = 0$	$J_{II} = 0$	$J_I = J_{II} = 0$	
Range-IV	Range-V	Range-VI	
$\pi/3 + \Delta\phi + \beta < \theta \leq 2\pi/3 - \Delta\phi + \beta$	$2\pi/3 - \Delta\phi + \beta < \theta \leq \pi + \beta$	$\pi + \beta < \theta \leq 4\pi/3 + \Delta\phi + \beta$	
$J_I = 0$	$J_I = J_{III} = 0$	$J_{III} = 0$	

Reprinted from Hasegawa et al. [31]. Copyright (2009) with permission from Elsevier

### 1.7.2 Governing Parameter for EM Damage at Polycrystalline Line Ends

Atom transport in a passivated metal line is assumed to be represented by Eq. (11). Boundary condition concerning the atomic diffusion at the metal line ends is taken into account; that is, there are no incoming and no outgoing flow of atoms at the line end. The boundary condition is set considering the microstructure unit region enclosed by a rectangle in Fig. 7. Let us consider the *AFD* in a unit region that faces the line end. First, the whole range of  $\theta$  (from 0 to  $2\pi$ ) is divided into six parts (Range-I to -VI), as shown in Table 1;  $\beta$  is defined as the angle between the line edge and the  $x$ -axis of the Cartesian coordinates shown in Fig. 7. Then, one or two atomic fluxes in three grain boundaries in the unit region are assumed to be zero for each  $\theta$ -range:  $J_{II} = J_{III} = 0$  in Range-I,  $J_{II} = 0$  in Range-II,  $J_I = J_{II} = 0$  in Range-III,  $J_I = 0$  in Range-IV,  $J_I = J_{III} = 0$  in Range-V and  $J_{III} = 0$  in Range-VI. Thus, the lack of incoming and outgoing atoms at the line ends can be considered by assigning a possible atomic flux of zero within the microstructure unit for each range of  $\theta$ . The atomic fluxes are summed within the unit. The sum is integrated with respect to  $\theta$  from 0 to  $2\pi$ , by distinguishing the six parts. The integrated value is finally multiplied by the cross-sectional area of the grain boundary,  $\delta$ , and divided by the volume of the unit region,  $\sqrt{3}d^2/4$  and by  $2\pi$ . In this way, the atomic flux

divergence at the ends of the passivated polycrystalline line is expressed by [30]

$$\begin{aligned}
 AFD_{\text{gen}}^*|_{\text{end}} &= \frac{2}{\sqrt{3}\pi d^2} \frac{C_{\text{gb}}^* N}{T} \exp\left(-\frac{Q_{\text{gb}} + \kappa\Omega(N - N_{\text{T}})/N_0 - \sigma_{\text{T}}\Omega}{kT}\right) \left\{ 6D_x \sin\beta - 6D_y \cos\beta \right. \\
 &\quad + \frac{\sqrt{3}}{4}\pi d \left[ -\frac{\kappa\Omega}{N_0} \left( \frac{\partial^2 N}{\partial x^2} + \frac{\partial^2 N}{\partial y^2} \right) - \frac{\kappa\Omega/N_0}{kT} \left( D_x \frac{\partial N}{\partial x} + D_y \frac{\partial N}{\partial y} \right) \right. \\
 &\quad \left. \left. + \frac{1}{T} \left( \frac{Q_{\text{gb}} + \kappa\Omega(N - N_{\text{T}})/N_0 - \sigma_{\text{T}}\Omega}{kT} - 1 \right) \left( D_x \frac{\partial T}{\partial x} + D_y \frac{\partial T}{\partial y} \right) \right] \right\}, \quad (58)
 \end{aligned}$$

where  $D_x = Z^* e \rho j_x - \kappa\Omega/N_0(\partial N/\partial x)$  and  $D_y = Z^* e \rho j_y - \kappa\Omega/N_0(\partial N/\partial y)$ . In Eq. (58),  $AFD_{\text{gen}}^*|_{\text{end}}$  denotes the governing parameter for EM damage at the ends of a passivated polycrystalline line.

### 1.7.3 AFD-Based Method for Derivation Utilizing Drift Velocity of Line End

The film's characteristic constants included in the AFD formula (Eq. (55)), are  $d$ ,  $\Delta\phi$ ,  $Q_{\text{gb}}$ ,  $Z^*$ ,  $C_{\text{gb}}^*$  and  $\kappa$ . The average grain size  $d$  can be measured by using a focused ion beam (FIB) system. We can obtain  $\Delta\phi$  experimentally by comparing an unpassivated metal line made of the same Al film as a passivated line [57]. The  $AFD_{\text{gen}}^*|_{\text{end}}$ -based method for determining the remaining constants considers a straight metal line. According to Blech [7, 8], the atomic density gradient in a straight metal line is inversely proportional to the length of the line. Stress measurements by Wang et al. [76, 77] indicate that the stress gradient during the initial stage of EM damage can be regarded as linear and independent of the given current density, provided that the input current density is less than several times the threshold current density. The product  $\kappa \cdot \partial N/\partial x$ , therefore, is considered to be a constant as a first approximation in the derivation method;  $\kappa \cdot \partial N/\partial x$  is derived as a characteristic constant depending on the length of the straight line. A current density considerably larger than the threshold current density should not be chosen for the experiment.

The film's characteristic constants  $Q_{\text{gb}}^*$  [ $=Q_{\text{gb}} - \sigma_{\text{T}}\Omega$ ],  $Z^*$ ,  $C_{\text{gb}}^*$  and  $\kappa \cdot \partial N/\partial x$  are determined by utilizing the drift velocity at the cathode end of the straight line. First, let us express the drift velocity by using  $AFD_{\text{gen}}^*|_{\text{end}}$ . Here, we introduce the effective length of the microstructure unit,  $l^*$  [ $=0.658d$ ], which is defined as the square root of the area of the microstructure unit,  $A$  [ $=\sqrt{3}d^2/4$ ]. We shall consider the  $l^* \times l^*$  square region at the cathode end (see Fig. 8). The  $x$ -axis is taken from the cathode end along the longitudinal direction of the line as shown in Fig. 8. At  $x = l^*$ , the average atomic flux  $J|_{x=l^*}$  is obtained by using  $AFD_{\text{gen}}^*|_{\text{end}}$ :

$$J|_{x=l^*} = \frac{AFD_{\text{gen}}^*|_{\text{end}}}{\delta} \frac{\sqrt{3}}{4} d^2. \quad (59)$$





measured drift velocity with the theoretical drift velocity in Eq. (61). In particular, the characteristic constants are determined such that the following sum of squares is minimized:

$$F_{\text{gb}}^*|_{\text{end}} = \sum_i \sum_j \left\{ v_{d|ij} - \left[ \left( AFD_{\text{gen}}^*|_{\text{end}} \right)_i + \left( \frac{\partial AFD_{\text{gen}}^*|_{\text{end}}}{\partial x} \right)_i (l_{d|ij} - l^*) \right] l^* \Omega \right\}^2. \quad (62)$$

Here, the subscripts  $i$  and  $j$  represent the condition number and the number of data measured in each experimental condition, respectively. By this method, the film's characteristic constants, namely,  $Q_{\text{gb}}^*$ ,  $Z^*$ ,  $C_{\text{gb}}^*$  and  $\kappa \cdot \partial N / \partial x$ , can be determined as optimized parameters that approximate all experimental data obtained from the measurement of drift velocity.

### 1.7.4 Experimental Procedure for Derivation

The metal lines used in the experiment were fabricated as shown in Fig. 9. Two specimens of different length, namely, Sample L and Sample S, were prepared. A TiN thin film was reactively sputtered onto a silicon substrate covered with silicon oxide; then, the Al film was continuously deposited on the TiN film by vacuum evaporation. The Al/TiN line specimens were patterned by conventional photolithography and etched by the reactive ion etching (RIE) technique. The small parts of both ends of the Al line were chemically etched and TiN layer was exposed, and thus the Al specimens modeled after the via-connected line were obtained. After that, tetraethyl orthosilicate (TEOS) film was deposited over the specimen's surface by plasma enhanced chemical vapor deposition (PE-CVD). An example of FIB observation of the Al grain microstructure is shown in Fig. 10. It was observed that the average grain size of the line specimen was 0.5  $\mu\text{m}$ .

**Fig. 9** Metal line specimen used in the experiment. Reprinted from Hasegawa et al. [31]. Copyright (2009) with permission from Elsevier

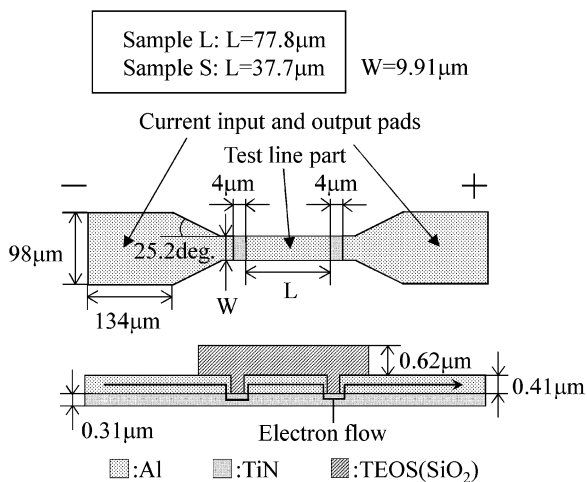
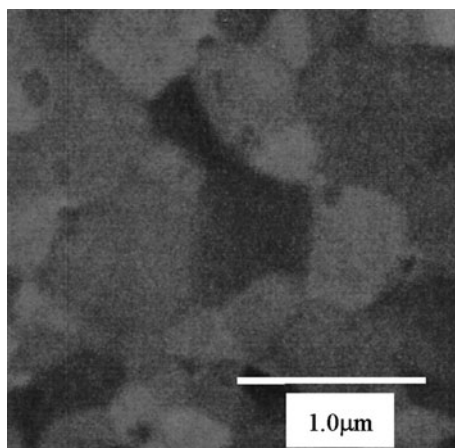


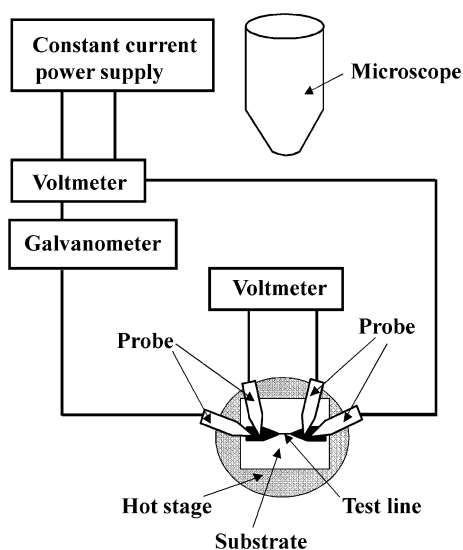
**Fig. 10** FIB observation of Al grain microstructure. Reprinted from Hasegawa et al. [31]. Copyright (2009) with permission from Elsevier



Instead of an actual via-connected line, a metal line modeled after the via-connected line was evaluated in this study. The line was evaluated without the via because of ease of fabrication, and because EM at the cathode end of the line is sufficiently produced in the specimen without using an actual via-connected line. The EM damage in the line specimen appears as the drift of the cathode end and as drift in the via-connected line. Blech [7, 8] and other researchers [48, 63] have often used similar line specimens.

The acceleration tests were performed by using the experimental set-up shown in Fig. 11. To measure the incubation period during which there was no void formation and no drift at the end, the change in the electrical potential drop across the line was monitored. The incubation period was defined from the start of current

**Fig. 11** Experimental setup for derivation. Reprinted from Hasegawa et al. [31]. Copyright (2009) with permission from Elsevier



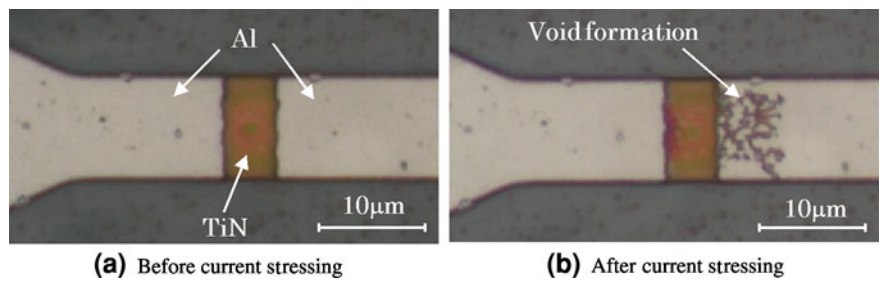


**Fig. 12** Observation of specimen’s cathode end by optical microscopy. Reprinted from Hasegawa et al. [31]. Copyright (2009) with permission from Elsevier

supply to the beginning of the increase in the electrical potential drop in the line as a result of void formation at the end. The net application time of electrical current,  $t_d$ , was obtained by subtracting the incubation period from the total application time. Three temperatures, namely, 508, 523 and 538 K, were selected as substrate temperatures. At each temperature, the metal lines of Sample L and Sample S were subjected to direct current with density of  $1.5 \text{ MA/cm}^2$  (Conditions 1, 2 and 3). In addition, the test was carried out at a current density of  $1.2 \text{ MA/cm}^2$  at substrate temperature of 538 K (Condition 4). Twelve specimens were used for each testing condition. After electric current was supplied until the potential drop increased 20 or 30%, the cathode end of the metal line was observed by optical microscopy, as shown in Fig. 12. The extent of void formation was evaluated by an image processing technique, and the drift length  $l_d$  was obtained by dividing the measured area by the line width. The drift length was then divided by the net time of current application. In this way, the drift velocity  $v_d$  was obtained from the experiment.

1.7.5 Results and Discussions of Derivation

The experimental data on drift velocity were substituted into Eq. (62) and the film’s unknown characteristic constants in  $AFD_{\text{gen}}^*|_{\text{end}}$  were optimized by using the least-squares method. The obtained constants are listed in Table 2. The value of  $Q_{\text{gb}}^*$  was close to the value of grain boundary diffusion [6, 7]. Furthermore, the value of  $Z^*$  appeared to be valid because it was within the range of the previously reported values,  $-1$  to  $-15$  [7, 8, 71, 76]. From a comparison of the values of  $Q_{\text{gb}}^*$  for Sample L and Sample S, it was found that the  $Q_{\text{gb}}^*$  values of these samples agreed well; thus, the constant  $Q_{\text{gb}}^*$  functioned as characteristic constant that was

**Table 2** Characteristic constants included in  $AFD_{\text{gen}}^*|_{\text{end}}$

	$Q_{\text{gb}}^*$ [eV]	$Z^*$	$C_{\text{gb}}^*$ [ $\text{K}\mu\text{m}^3/\text{Js}$ ]	$\kappa \cdot \partial N/\partial x$ [ $\text{J}/\mu\text{m}^7$ ]
Sample L	0.55	−8.3	$2.7 \times 10^{24}$	0.36
Sample S	0.54	−8.4	$2.4 \times 10^{24}$	0.86

Reprinted from Hasegawa et al. [31]. Copyright (2009) with permission from Elsevier

independent of the line length and dependent on only film characteristics. The amount of vacancies at the grain boundary depends on the purity of the material, and a higher vacancy concentration directly contributes to a higher diffusion coefficient. Accordingly, mass transport is more easily induced in films with low activation energy [80].

Comparing  $Z^*$  and  $C_{gb}^*$  of Sample L with those of Sample S, it is found that these values are almost the same. Therefore, the constants  $Z^*$  and  $C_{gb}^*$  also serve as characteristic constants independent of line length. On the other hand, the  $\kappa \cdot \partial N / \partial x$  value of Sample S is more than twice as large as that of Sample L, and only the  $\kappa \cdot \partial N / \partial x$  value in Table 2 appeared to depend on line length. According to Blech [7], the atomic density gradient is inversely proportional to line length. Therefore,  $\kappa \cdot \partial N / \partial x$  functioned appropriately as a characteristic constant that depends on line length; consequently, the quantity  $\kappa$  was thought to act as a constant independent of the line-length. Hence, it was concluded that the film's characteristic constants were appropriately determined by the  $AFD_{gen|end}^*$ -based method.

The effective bulk modulus,  $\kappa$ , the critical atomic density for void initiation,  $N_{min}^*$ , and the critical atomic density for hillock initiation,  $N_{max}^*$ , are obtained by a numerical simulation for the process of building up the atomic density distribution [62]. The values of  $\kappa$ ,  $N_{min}^*$  and  $N_{max}^*$  are determined by simulation of atomic density distribution for the incubation period, during which no EM damage appears [61]. The simulation is carried out during the incubation period measured in the acceleration test. The quantity  $\kappa$  is determined such that the product of  $\kappa$  assumed in the simulation and the atomic density gradient after the simulation agrees with the value of  $\kappa \cdot \partial N / \partial x$  obtained from the  $AFD_{gen|end}^*$ -based method. Then, we obtain the atomic density distribution in the line after the incubation period through the simulation using the determined  $\kappa$  value. The smallest value of atomic density depending on  $\theta$  [62],  $N^*$ , in the line is defined as  $N_{min}^*$ , and the largest value as  $N_{max}^*$ .

The previous method for deriving the film's characteristic constants based on the parameter  $AFD_{gen}^*$  required the observation of void formation by a scanning electron microscopy (SEM) after removal of the passivation layer [61]. In contrast, the present  $AFD_{gen|end}^*$ -based method based on drift velocity measurements can be carried out without removal of the passivation layer and requires only the observation of the cathode end by optical microscopy. Thus, the  $AFD_{gen|end}^*$ -based method presented here is not only accurate but also much easier than the  $AFD_{gen}^*$ -based method.

## 2 Stress Migration

### 2.1 Introduction

SM is another failure mechanism that is often referred to, together with EM, in the study of reliability issues for interconnection systems. With the development of

ultra-large-scale integration for semiconductors, the minimum dimensions for interconnects have been reduced to the sub-micron range. For such small-sized but full-featured devices, multilevel metallization is required. As a result, some unexpected influences have occurred to accompany the introduction of layered conducting lines. Apart from the EM-induced mass transport that occurs due to high density electron flow, residual stress is also generated in thermal processing when there is a difference in thermal expansion coefficients or a chemical reaction between the bonded elements, and so on. At times, these stresses can develop to a level that causes atomic diffusion to the extent where they lead to structural changes, typical known as examples being whisker growth and stress induced voids [11, 13, 15, 18, 19, 54, 70]. If the whiskers that are generated are long enough to connect two conductive layers, or if the voids grow to the dimensions of the line widths, these will result in short circuits or electrical discontinuities, respectively. Here, some typical phenomena relevant to SM will be reviewed in the following sections.

## ***2.2 Historical Review of Typical SM-Induced Phenomena***

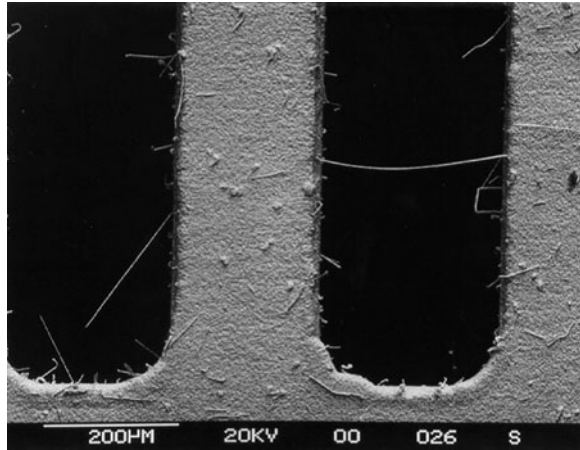
### **2.2.1 Spontaneous Sn Whisker Growth**

During World War II the electroplated material of choice for electrical components was electroplated cadmium (Cd). Repeated failures of electrical hardware led to a finding that many failures were due to shorting from Cd whiskers [27]. These findings were summarized by Cobb [17], and it was the first report concerning the problems of whisker growth. Starting in 1948, similar failures were experienced by Bell Telephone on the channel filters used for multi-channel transmission lines. Bell Laboratories immediately initiated the use of pure Sn electroplating to replace Cd, but they quickly found that pure Sn also had whisker problems similar to those experienced with Cd plating [18]. Since then, Sn whisker research has attracted considerable attention over 50 years due to the Sn and Sn-based alloys that have been widely used in the electronic industry until now. Figure 13 shows a typical example of a Sn whisker-induced reliability issue. As shown in the figure, many whiskers grew on a eutectic SnCu finish on a leadframe. One of the whiskers is so long that it has bridged a pair of the legs.

It is striking to note that essentially all of the fundamental concepts still debated today were initially established during the 1950s. Many of these 1950s era proposals were perhaps little more than well-informed speculation at the time, but they were based on sound principles of materials science and they formed a basis for all current discussion relevant to whisker formation [27]. Some highlights of this research are worthy of further review, as listed below:

- (1) As reported in Bell Laboratories' work published in 1951, whisker growth was recognized as a spontaneous process, not only on Cd, Zn and Sn electroplating, but also on Al casting alloys and Ag electroplating exposed to an atmosphere of hydrogen sulfide [18].

**Fig. 13** SEM image of Sn whiskers grown on eutectic SnCu finish on a leadframe. One of the whiskers shorts two of the leadframe legs [78]



- (2) Herring and Galt [34] inferred that Sn whiskers were single crystals without lattice defects by investigating their elastic and plastic properties.
- (3) By showing electron micrographs of the different stages in the growth of Sn whiskers, Koonce and Arnold [41] established the fact that Sn whisker growth took place as a result of the addition of material at the base, rather than at the tip.
- (4) Fisher et al. [24] established that compressive stress gradients were the driving force for whisker growth. This knowledge has made such a great contribution to the subsequent proposed whisker growth models.

Going through several decades of research assisted by experimental tools that have been developed over the years, Sn whisker growth has been confirmed as a spontaneous process, driven by a compressive stress gradient, growing from the base, and readily occurring at room temperature. However, the mechanism is still unclear to date. Several models have been constructed to describe the mechanism of Sn whisker growth. Dislocation-based theories have been proposed independently by Eshelby [22], Frank [25], Amelinckx et al. [3] and Lee and Lee [43]. Recrystallization-based theories were proposed by Ellis et al. [21], and subsequently developed by Furuta and Hamamura [26]. In 1973, Tu [70] published his paper on Sn whisker growth. As reported in his paper, Sn whiskers were observed at room temperature growing from the Sn surfaces of Cu–Sn bimetallic films, but not at Sn films without a Cu under-layer. This was attributed to a driving force generated by the formation of  $\text{Cu}_6\text{Sn}_5$  intermetallic compounds (IMCs) in the Cu–Sn films [70]. Later, Tu and co-authors have demonstrated the existence of IMC by utilizing new analytical techniques such as TEM and FIB examinations. In addition, Tu [72] proposed that the oxide layer on the Sn film played a dominant role in affecting Sn whisker growth. Weak spots in the oxide layer are important in enabling local stress relaxation to form Sn whiskers. Without the surface oxide, a homogeneous relaxation occurs over the entire film [72]. This theory can be well understood from a comparison of the illustrations shown in Figs. 14 and 15. Besides the models mentioned above, a great deal of important data has been

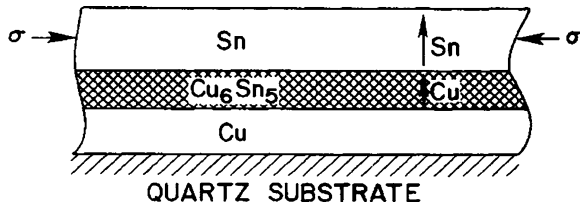
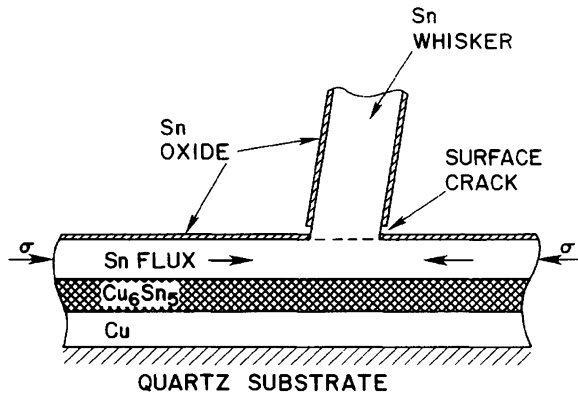


**Fig. 14** A sketch of the cross section of the bimetallic Cu–Sn thin films forming the compound  $\text{Cu}_6\text{Sn}_5$ . The surface of Sn is assumed to be free of oxide. The arrows indicate the fluxes in the Sn and the compound. Reprinted with permission from Tu [71]. Copyright 1994 by the American Physical Society

**Fig. 15** A sketch of the cross section of the bimetallic Cu–Sn thin films forming the compound  $\text{Cu}_6\text{Sn}_5$  and a whisker. The surfaces of the Sn and the whisker are oxidized except the base of the whisker where the oxide is broken. A lateral flux of Sn is indicated by arrows in the Sn film. Reprinted with permission from Tu [72]. Copyright 1994 by the American Physical Society



reported, as represented by Zhang et al. [79], Choi et al. [16], Barsoum et al. [4] and Galyon and Palmer [28].

The SM-induced reliability issue has been the main driver for these studies ever since the whisker problem was discovered. With the ongoing reduction of circuit feature sizes, it is increasingly relevant to the electronic packaging industries. Most of the correlative works focus on suppressing whisker growth as far as possible. It is noted that one may consider ways such as the creation of an environment in which no natural oxide layer is formed on the surface of the material, or covering the surface of the material with a tough artificial layer [69], for the suppression of whisker formation.

### 2.2.2 Fabrication of Nanowires by Utilizing Controllable SM

With the newly reported works on various nanowires fabricated by utilizing SM [15, 35, 51, 54, 64, 66], the field of SM research has entered a new phase, not only in terms of its suppression, but also in terms of its applications. This is because one-dimensional nano-structures have attracted considerable attention due to their unique mechanical, electrical, and magnetic properties, and their fundamental importance to MEMS/NEMS in recent years.

It has been demonstrated that whisker growth is driven by compressive stress gradients. The origin of the compressive stress can be mechanical, thermal, and chemical [78]. Based on the opinion of Tu [70], in order for Sn whiskers to grow, there must be a chemical reaction between the bonded elements to guarantee the necessary stress generation. Moreover, because Sn whisker growth is a spontaneous process, the stress that is generated is internal and so the geometrical properties of whiskers are uncontrollable. All of the characteristics described above have certain limitations that must be taken into account in consideration of nanowire formation by utilizing SM, such as the choice of source material, the growth rate, the generation of the driving force and controllability.

In contrast to ‘traditional’ Sn whisker growth, alternative approaches have been developed in which an external applied stress is used to induce atomic diffusion. Almost all of these fabrication techniques aimed at utilizing the thermal stresses that result from a mismatch in thermal expansion coefficients in bilayer/multilayer structures. Let us refer to the work by Shim et al. [66] to give a schematic representation of the nanowire growth mechanism. Taking Bi nanowire growth as an example, and as illustrated in Fig. 16a, a trilayer structure with an oxidized Si substrate followed by a Bi layer is used. It should be mentioned that there is a large difference between the thermal expansion coefficients of Bi ( $13.4 \mu\text{m m}^{-1} \text{K}^{-1}$ ) and  $\text{SiO}_2/\text{Si}$  ( $0.5 \mu\text{m m}^{-1} \text{K}^{-1}/2.4 \mu\text{m m}^{-1} \text{K}^{-1}$ ). The Bi film expands while it is annealed in the temperature range  $260\text{--}270^\circ\text{C}$ , while the substrate restricts expansion, putting the Bi film under compressive stress [66]. By making use of stress relief and atomic diffusion, Bi nanowires can be fabricated. The mass of Bi nanowires that are formed have high aspect ratios (length/diameter), as shown in Fig. 16b. Figure 16c shows TEM analysis of a formed Bi nanowire. The nanowire was found to be uniform in diameter and to have formed a 10 nm thick Bi oxide layer on its outer surface [66]. The presence of the Bi oxide layer seems to agree well with the oxide layer theory proposed by Tu [72]. The effect of the oxide layer on stress-induced extrusion was also studied by other researchers [14, 15, 38].

It is noteworthy that the growth of SM-induced nanowires is governed by temperature, film thickness, grain size and the time that the film is subjected to stress during the process [54]. Therefore, by adjusting these parameters, the growth of nanowires can be controlled. This seems to be especially important in order to achieve higher aspect ratios, or the rapid and mass growth of these nanowires. Although the current technique for the fabrication of nanowires by utilizing SM is imperfect, we can expect it to be applied to mass production process in industry in the near future.

## 2.3 Summary

Since the atomic diffusion induced by SM is a stress relief phenomenon, it must relate to the stress gradient. To be precise, it occurs due to a gradient of compressive hydrostatic stress. Denoting the hydrostatic stress by  $\sigma$  and considering a



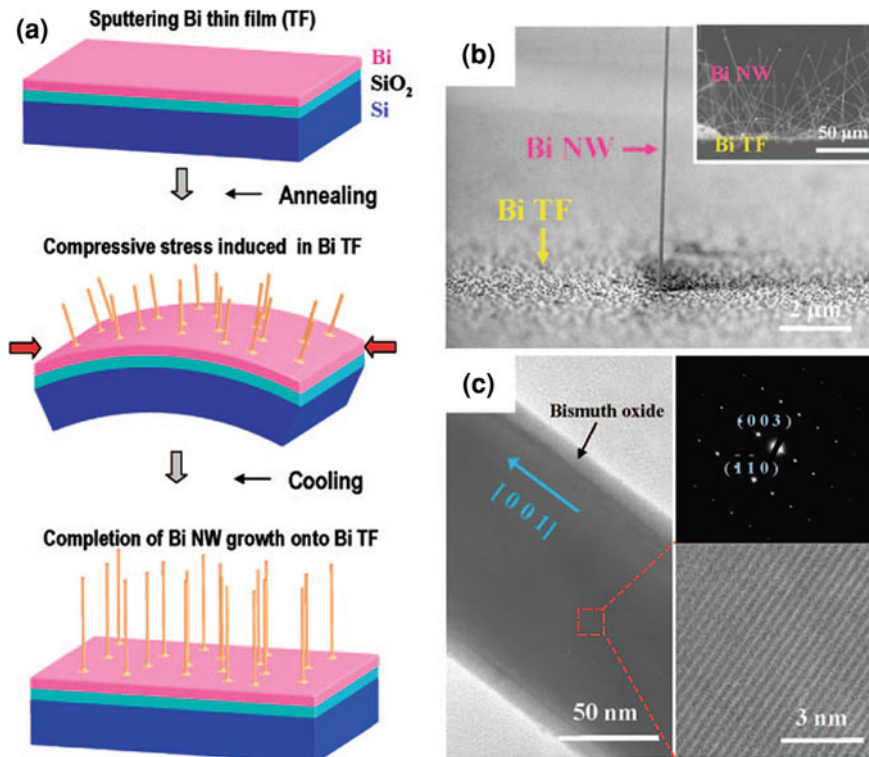
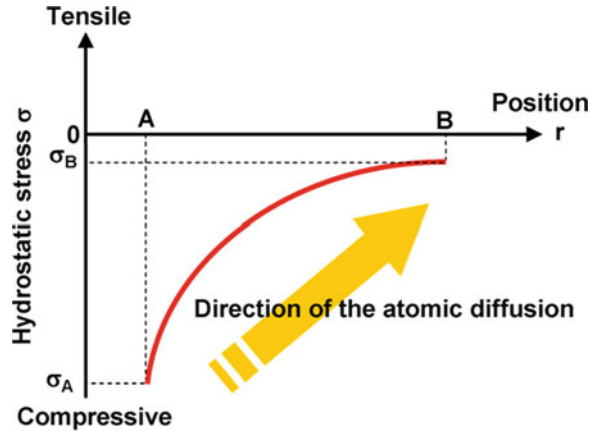


**Fig. 16** Growth mechanism and structural characteristic of the single-crystalline Bi nanowires. **a** a schematic representation of the growth of Bi nanowires by on-film formation of nanowires, **b** a SEM image of a Bi nanowire grown on a Bi thin film, and **c** a low-magnification TEM image of a Bi nanowire [66]

material with a distribution of compressive stress as shown in Fig. 17, the atoms diffuse from position A with more-negative stress (higher compressive stress) towards position B with less-negative stress (lower compressive stress). As a result, a local atomic accumulation is caused at position B. The hydrostatic stress is expressed as  $\sigma = (\sigma_x + \sigma_y + \sigma_z)/3$ , where  $\sigma_x$ ,  $\sigma_y$  and  $\sigma_z$  are the corresponding normal stresses in the Cartesian coordinates system ( $x$ ,  $y$ ,  $z$ ). In most of these cases, the surface of a material subjected to SM is covered by an oxide layer or by a passivation layer. In those cases, the normal stresses  $\sigma_x$ ,  $\sigma_y$  and  $\sigma_z$  caused by the accumulation of atoms are the same as each other,  $\sigma_x = \sigma_y = \sigma_z$ , and hence  $\sigma$  is equal to  $\sigma_x$ , where  $x$  is usually taken in the longitudinal direction of the tested material and  $z$  is in the normal direction to the surface of the material. The SM-induced atomic flux,  $\mathbf{J}_S$  is given by [33, 42]

$$\mathbf{J}_S = \frac{N\Omega D_0}{kT} \exp\left(-\frac{Q - \Omega\sigma}{kT}\right) \text{grad}\sigma \quad (63)$$

**Fig. 17** Illustration for the phenomenon of SM in a material with a distribution of compressive stress. Reprinted with permission from Saka et al. [55]. © 2008 IEEE



Here, the gradient of  $\sigma$  is the driving force for atomic diffusion, and this differs with the electron flow, which is used to describe that of EM.

**Acknowledgments** K. S. acknowledges T. Abo for his help in preparing the manuscript. M. S. wishes to express his thanks to X. Zhao for his kind help in preparing the manuscript.

## References

1. Abé, H., Sasagawa, K., Saka, M.: Electromigration failure of metal lines. *Int. J. Fract.* **138**, 219–240 (2006)
2. Ainslie, N.G., d’Heurle, F.M., Wells, O.C.: Coating, mechanical constraints, and pressure effects on electromigration. *Appl. Phys. Lett.* **20**, 173–174 (1972)
3. Amelinckx, S., Bontinck, W., Dekeyser, W., Seitz, F.: On the formation and properties of helical dislocations. *Phil. Mag.* **2**, 355–377 (1957)
4. Barsoum, M.W., Hoffman, E.N., Doherty, R.D., Gupta, S., Zavaliangos, A.: Driving force and mechanism for spontaneous metal whisker formation. *Phys. Rev. Lett.* **93**, 206104 (1-4) (2004)
5. Black, J.R.: Electromigration—a brief survey and some recent results. *IEEE Trans. Electron Devices* **ED-16**, 338–347 (1969)
6. Black, J.R.: Electromigration failure modes in aluminum metallization for semiconductor devices. *Proc. IEEE* **57**, 1587–1593 (1969)
7. Blech, I.A.: Electromigration in thin aluminum films on titanium nitride. *J. Appl. Phys.* **47**, 1203–1208 (1976)
8. Blech, I.A.: Diffusional back flows during electromigration. *Acta Mater.* **46**, 3717–3723 (1998)
9. Blech, I.A., Herring, C.: Stress generation by electromigration. *Appl. Phys. Lett.* **29**, 131–133 (1976)
10. Blech, I.A., Meieran, E.S.: Electromigration in thin Al films. *J. Appl. Phys.* **40**, 485–491 (1969)
11. Blech, I.A., Petroff, P.M., Tai, K.L., Kumar, V.: Whisker growth in Al thin films. *J. Cryst. Growth.* **32**, 161–169 (1975)
12. Böhm, J., Volkert, C.A., Mönig, R., Balk, T.J., Arzt, E.: Electromigration-induced damage in bamboo Al interconnects. *J. Electron. Mater.* **31**, 45–49 (2002)

13. Børgesen, P., Lee, J.K., Gleixner, R., Li, C.-Y.: Thermal-stress-induced voiding in narrow, passivated Cu lines. *Appl. Phys. Lett.* **60**, 1706–1708 (1992)
14. Chang, C.Y., Vook, R.W.: The effect of surface aluminum oxide films on thermally induced hillock formation. *Thin Solid Films* **228**, 205–209 (1993)
15. Cheng, Y.-T., Weiner, A.M., Wong, C.A., Balogh, M.P.: Stress-induced growth of bismuth nanowires. *Appl. Phys. Lett.* **81**, 3248–3250 (2002)
16. Choi, W.J., Lee, T.Y., Tu, K.N., Tamura, N., Celestre, R.S., McDowell, A.A., Bong, Y.Y., Liu, N.: Tin whiskers studied by synchrotron radiation scanning X-ray micro-diffraction. *Acta Mater.* **51**, 6253–6262 (2003)
17. Cobb, H.L.: Cadmium whiskers. *Mon. Rev. Am. Electroplaters Soc.* **33**, 28–30 (1946)
18. Compton, K.G., Mendizza, A., Arnold, S.M.: Filamentary growths on metal surfaces—Whiskers. *Corrosion* **7**, 327–334 (1951)
19. Curry, J., Fitzgibbon, G., Guan, Y., Muollo, R., Nelson, G., Thomas, A.: New failure mechanisms in sputtered aluminum-silicon films. *IEEE Proc. Int. Reliab. Phys. Symp.* **22**, 6–8 (1984)
20. d’Heurle, F., Ames, I.: Electromigration in single crystal aluminum films. *Appl. Phys. Lett.* **16**, 80–81 (1970)
21. Ellis, W.C., Gibbons, D.F., Treuting, R.C.: Growth of Metal Whiskers from the Solid. *Growth and Perfection of Crystals*, pp. 102–120. Wiley, New York (1958)
22. Eshelby, J.D.: A tentative theory of metallic whisker growth. *Phys. Rev.* **91**, 755–756 (1953)
23. Fiks, V.B.: On the mechanism of the mobility of ions in metals. *Sov. Phys. Solid State* **1**, 14–28 (1959)
24. Fisher, R.M., Darken, L.S., Carroll, K.G.: Accelerated growth of tin whiskers. *Acta Metall.* **2**, 368–373 (1954)
25. Frank, F.C.: On tin whiskers. *Phil. Mag.* **44**, 854–860 (1953)
26. Furuta, N., Hamamura, K.: Growth mechanism of proper tin-whisker. *Jpn. J. Appl. Phys.* **8**, 1404–1410 (1969)
27. Galyon, G.T.: A History of Tin Whisker Theory: 1946 to 2004. SMTA International Conference, Chicago (2004)
28. Galyon, G.T., Palmer, L.: An integrated theory of whisker formation: the physical metallurgy of whisker formation and the role of internal stresses. *IEEE Trans. Elect. Packag. Manuf.* **28**, 17–30 (2005)
29. Gonzalez, J.L., Rubio, A.: Shape effect on electromigration in VLSI interconnects. *Microelectron Reliab.* **37**, 1073–1078 (1997)
30. Hasegawa, M., Sasagawa, K., Saka, M., Abé, H.: Expression of a governing parameter for electromigration damage on metal line ends. In: *Proceedings of the ASME InterPACK ‘03(CD-ROM): InterPack 2003-35064* (2003)
31. Hasegawa, M., Sasagawa, K., Uno, S., Saka, M., Abé, H.: Derivation of film characteristic constants of polycrystalline line for reliability evaluation against electromigration failure. *Mech. Mater.* **41**, 1090–1095 (2009) (See corrigendum to this article, Doi: [10.1016/j.mechmat.2010.09.004](https://doi.org/10.1016/j.mechmat.2010.09.004), for Table 2)
32. Hau-Riege, S.P., Thompson, C.V.: Experimental characterization and modeling of the reliability of interconnect trees. *J. Appl. Phys.* **89**, 601–609 (2001)
33. Herring, C.: Diffusional viscosity of a polycrystalline solid. *J. Appl. Phys.* **21**, 437–445 (1950)
34. Herring, C., Galt, J.K.: Elastic and plastic properties of very small metal specimens. *Phys. Rev.* **85**, 1060–1061 (1952)
35. Hinode, K., Homma, Y., Sasaki, Y.: Whiskers grown on aluminum thin films during heat treatments. *J. Vac. Sci. Technol. A* **14**, 2570–2576 (1996)
36. Hu, C.-K., Small, M.B., Rodbell, K.P., Stanis, C., Blauner, P., Ho, P.S.: Electromigration failure due to interfacial diffusion in fine Al alloy lines. *Appl. Phys. Lett.* **62**, 1023–1025 (1993)
37. Huntington, H.B., Grone, A.R.: Current-induced marker motion in gold wires. *J. Phys. Chem. Solids* **20**, 76–87 (1961)
38. Iwamura, E., Takagi, K., Ohnishi, T.: Effect of aluminum oxide caps on hillock formation in aluminum alloy films. *Thin Solid Films* **349**, 191–198 (1999)

39. Kawamura, M., Mashima, T., Abe, Y., Sasaki, K.: Formation of ultra-thin continuous Pt and Al film by RF sputtering. *Thin Solid Films* **377–378**, 537–542 (2000)
40. Kirchheim, R., Kaerber, U.: Atomistic and computer modeling of metallization failure of integrated circuits by electromigration. *J. Appl. Phys.* **70**, 172–181 (1991)
41. Koonce, S.E., Arnold, S.M.: Growth of metal whiskers. *J. Appl. Phys.* **24**, 365–366 (1953)
42. Korhonen, M.A., Børgesen, P., Tu, K.N., Li, C.-Y.: Stress evolution due to electromigration in confined metal lines. *J. Appl. Phys.* **73**, 3790–3799 (1993)
43. Lee, B.-Z., Lee, D.N.: Spontaneous growth mechanism of tin whiskers. *Acta Mater.* **46**, 3701–3714 (1998)
44. Lloyd, J.R., Smith, P.M.: The effect of passivation thickness on the electromigration lifetime of Al/Cu thin film conductors. *J. Vac. Sci. Technol. A* **1**, 455–458 (1983)
45. Marcoux, P.J., Merchant, P.P., Naroditsky, V., Rehder, W.D.: New 2D simulation model of electromigration. Hewlett-Packard J. 79–84 (June 1989)
46. Nikawa, K.: Monte Carlo calculations based on the generalized electromigration failure model. *Proc. 19th IEEE Int. Reliab. Phys. Symp.* 175–181 (1981)
47. Oates, A.S.: Electromigration in multilayer metallization: drift-controlled degradation and the electromigration threshold of Al–Si–Cu/TiN<sub>x</sub>O<sub>y</sub>/TiSi<sub>2</sub> contacts. *J. Appl. Phys.* **70**, 5369–5373 (1991)
48. Oates, A.S.: Electromigration transport mechanisms in Al thin-film conductors. *J. Appl. Phys.* **79**, 163–169 (1996)
49. Oates, A.S., Barr, D.L.: Lattice electromigration in narrow Al alloy thin-film conductors at low temperatures. *J. Electron. Mater.* **23**, 63–66 (1994)
50. Park, Y.J., Thompson, C.V.: The effects of the stress dependence of atomic diffusivity on stress evolution due to electromigration. *J. Appl. Phys.* **82**, 4277–4281 (1997)
51. Prokes, S.M., Arnold, S.: Stress-driven formation of Si nanowires. *Appl. Phys. Lett.* **86**, 193105 (1–3) (2005)
52. Proost, J., Maex, K., Delaey, L.: Electromigration-induced drift in damascene and plasma-etched Al(Cu). II. Mass transport mechanisms in bamboo interconnects. *J. Appl. Phys.* **87**, 99–109 (2000)
53. Renucci, P., Gaudart, L., Petrakian, J.P., Roux, D.: New model for the temperature coefficient of resistivity of polycrystalline films: application to alkaline-earth metals. *J. Appl. Phys.* **54**, 6497–6501 (1983)
54. Saka, M., Yamaya, F., Tohmyoh, H.: Rapid and mass growth of stress-induced nanowhiskers on the surfaces of evaporated polycrystalline Cu films. *Scr. Mater.* **56**, 1031–1034 (2007)
55. Saka M, Yasuda M, Tohmyoh H, Settsu N, Fabrication of Ag micromaterials by utilizing stress-induced migration. In: *Proc. 2nd Electronics Systemintegration Technology Conference* © 2008 IEEE (2008)
56. Sasagawa, K., Saka, M., Abé, H.: Current density and temperature distributions near the corner of angled metal line. *Mech. Res. Commun.* **22**, 473–483 (1995)
57. Sasagawa, K., Nakamura, N., Saka, M., Abé, H.: A new approach to calculate atomic flux divergence by electromigration. *Trans. ASME J. Electron. Packag.* **120**, 360–366 (1998)
58. Sasagawa, K., Naito, K., Saka, M., Abé, H.: A method to predict electromigration failure of metal lines. *J. Appl. Phys.* **86**, 6043–6051 (1999)
59. Sasagawa, K., Naito, K., Kimura, H., Saka, M., Abé, H.: Experimental verification of prediction method for electromigration failure of polycrystalline lines. *J. Appl. Phys.* **87**, 2785–2791 (2000)
60. Sasagawa, K., Hasegawa, M., Saka, M., Abé, H.: A governing parameter for electromigration damage in passivated polycrystalline line and its verification. In: Baker, S.P. (ed.) *Stress-induced Phenomena in Metallization* 612. AIP, Melville (2001)
61. Sasagawa, K., Hasegawa, M., Saka, M., Abé, H.: Governing parameter for electromigration damage in the polycrystalline line covered with a passivation layer. *J. Appl. Phys.* **91**, 1882–1890 (2002)
62. Sasagawa, K., Hasegawa, M., Saka, M., Abé, H.: Prediction of electromigration failure in passivated polycrystalline line. *J. Appl. Phys.* **91**, 9005–9014 (2002)

63. Schreiber, H.-U.: Electromigration mechanisms in aluminum lines. *Solid-State Electron* **28**, 1153–1163 (1985)
64. Settsu, N., Saka, M., Yamaya, F.: Fabrication of Cu nanowires at predetermined positions by utilizing stress migration. *Strain* **44**, 201–208 (2008)
65. Shewmon, P.: *Diffusion in Solids*. Minerals Metals and Materials Society, Warrendale (1989)
66. Shim, W., Ham, J., Lee, K., Jeung, W.Y., Johnson, M., Lee, W.: On-film formation of Bi nanowires with extraordinary electron mobility. *Nano Lett.* **9**, 18–22 (2009)
67. Shin, W.C., Besser, R.S.: A micromachined thin-film gas flow sensor for microchemical reactors. *J. Micromech. Microeng.* **16**, 731–741 (2006)
68. Shingubara, S., Nakasaki, Y., Kaneko, H.: Electromigration in a single crystalline submicron width aluminum interconnection. *Appl. Phys. Lett.* **58**, 42–44 (1991)
69. Tohmyoh, H., Yasuda, M., Saka, M.: Controlling Ag whisker growth using very thin metallic films. *Scr. Mater.* **63**, 289–292 (2010)
70. Tu, K.N.: Interdiffusion and reaction in bimetallic Cu-Sn thin films. *Acta Metall.* **21**, 347–354 (1973)
71. Tu, K.N.: Electromigration in stressed thin films. *Phys. Rev. B* **45**, 1409–1413 (1992)
72. Tu, K.N.: Irreversible processes of spontaneous whisker growth in bimetallic Cu–Sn thin-film reactions. *Phys. Rev. B* **49**, 2030–2034 (1994)
73. Vaidya, S., Sheng, T.T., Sinha, K.: Linewidth dependence of electromigration in evaporated Al-0.5%Cu. *Appl. Phys. Lett.* **36**, 464–466 (1980)
74. Villars, P.: *Pearson's Handbook Desk Edition—Crystallographic Data for Intermetallic Phases*, 1. ASM International, Material Park (1997)
75. Walton, D.T., Frost, H.J., Thompson, C.V.: Development of near-bamboo and bamboo microstructures in thin-film strips. *Appl. Phys. Lett.* **61**, 40–42 (1992)
76. Wang, P.-C., Cargill III, G.S., Noyan, I.C., Hu, C.-K.: Electromigration-induced stress in aluminum conductor lines measured by X-ray microdiffraction. *Appl. Phys. Lett.* **72**, 1296–1298 (1998)
77. Wang, P.-C., Noyan, I.C., Kaldor, S.K., Jordan-Sweet, J.L., Liniger, E.G., Hu, C.-K.: Topographic measurement of electromigration-induced stress gradients in aluminum conductor lines. *Appl. Phys. Lett.* **76**, 3726–3728 (2000)
78. Zeng, K., Tu, K.N.: Six cases of reliability study of Pb-free solder joints in electronic packaging technology. *Mater. Sci. Eng. R* **38**, 55–105 (2002)
79. Zhang, Y., Xu, C., Fan, C., Vysotskaya, A., Abys, J.: Understanding whisker phenomenon—Part I: Growth rate. In: *Proc. of the 2001 AESF SUR/FIN Conf.: NA* (2001)
80. Zhao, X., Saka, M., Yamashita, M., Togoh, F.: Evaluation of the dominant factor for electromigration in sputtered high purity Al films. *Trans. ASME J. Electron. Packag.* **132**, 021003 (1–9) (2010)



<http://www.springer.com/978-3-642-15410-2>

Metallic Micro and Nano Materials

Fabrication with Atomic Diffusion

Saka, M. (Ed.)

2011, X, 238 p., Hardcover

ISBN: 978-3-642-15410-2